A STUDY ON THE CORROSION BEHAVIOR OF NANOCRYSTALLINE NICKEL IN AQUEOUS ENVIRONMENTS

by

ANJANA SHYAM SUNDAR

Presented to the Faculty of the Graduate School of

The University of Texas at Arlington in Partial Fulfillment

of the Requirements

for the Degree of

MASTER OF SCIENCE IN MATERIALS SCIENCE AND ENGINEERING

THE UNIVERSITY OF TEXAS AT ARLINGTON

December 2010

To

God,

My parents, brother

and my uncle

ACKNOWLEDGEMENTS

"At times our own light goes out and is rekindled by a spark from another person. Each of us has cause to think with deep gratitude of those who have lighted the flame within us." -Albert Schweitzer

I take this opportunity to express my sincere gratitude to my mentor and guide Dr. Efstathios I. Meletis who has always been supportive and encouraged me during the course of my research work. His inspiring words on striving hard for success, never give up attitude have imbibed in me for the rest of my life.

I would like to thank Mr. Kermit Beird, who has helped in machining my samples. I would like to thank Dr. J. Jiang for helping me with the profilometry analysis. I extend my appreciation to my committee members Dr. Pranesh Aswath and Dr. Fuqiang Liu for their time, effort and patience. I would also like to appreciate the help from Ms. Jennifer Standlee and Libia Cuauhalti for helping me with all the department formalities and paper work. A special thanks to all my group members, especially Dr. Cristian Cionea, Yinsheng Fang, Razieh Khalifehzadeh, Jie He, for their words of encouragement, helping me with practical work and troubleshooting problems. I thank all my friends for their moral support, especially Mr. Vinay Vikram.

I am very grateful to my parents, Mr. Shyamsundar and Mrs. Jayashree Shyamsundar, my uncle Mr. Vijay Kumar, my brother Mr. Adarsh Shyamsundar and sister in law Mrs. Reena Patel for their unconditional love and support throughout my life.

December 15, 2010

ABSTRACT

A STUDY ON THE CORROSION BEHAVIOR OF NANOCRYSTALLINE NICKEL

IN AQUEOUS ENVIRONMENTS

Anjana Shyamsundar, M.S

The University of Texas at Arlington, 2010

Supervising Professor: Efstathios I Meletis

Nanocrystalline materials possess considerably enhanced properties arising from their small grain size. Significant interest has been paid in the past to their mechanical and physical properties. Very little attention has been attracted by their electrochemical behavior, which is expected to be affected by the significant volume fraction of grain boundaries. In the present study, corrosion experiments were conducted in nanocrystalline nickel in two entirely different solutions in order to obtain a better understanding of its corrosion behavior. This is of particular interest to MEMS and NEMS devices where electroplated nanocrystalline nickel is the metal of choice.

The corrosion behavior of bulk (microcrystalline) and nanocrystalline Ni were studied in 3.5% NaCl and 0.1N H_2SO_4 aerated and deaerated solutions. Potentiodynamic polarization and open circuit potential *vs* time experiments were conducted to observe the corrosion behavior in a pitting environment (3.5% NaCl solution) and a passivating environment (0.1N H_2SO_4). The surface morphology after corrosion testing was analyzed using scanning electron microscopy (SEM) and optical profilometry. The bulk and nano Ni were characterized using X-ray diffraction (XRD) and energy dispersive X-ray spectroscopy (EDS) to determine the grain size and composition, respectively.

Nano Ni was found to exhibit a more noble potential in both NaCl and H_2SO_4 solutions compared to its microcrystalline counterpart. In aerated environments, the corrosion rate of nano Ni was significantly higher than that of bulk Ni. This was attributed to the catalytic properties exhibited by the large volume fraction of grain boundaries present in nano Ni in terms of facilitating the oxygen reduction action. In deaerated solutions, nano Ni exhibits either a significantly lower (i.e., NaCl solution) or comparable (i.e., 0.1N H_2SO_4 solution) corrosion rate to that of its microcrystalline counterpart. In terms of surface morphology pits in nano Ni tested in NaCl solution, were found to be uniform in depth ~42 μm, whereas microcrystalline Ni showed a large variation extending to a depth of 59 μm). In the diluted H_2SO_4 solution, bulk Ni exhibited passivation behavior whereas nano Ni was not passivated but, corrosion found to be rather uniform. Nanocrystalline Ni was not able to passivate due to its high density of surface defects inhibiting stable oxide formation.

A bimodal pit distribution was observed in nano Ni tested in NaCl solution consisting of numerous submicron pits and a small number of dispersed larger pits. The formation of the latter pits was found to involve both vertical and lateral growth in view of the high density of grain boundaries that provide sensitive sites.

TABLE OF CONTENTS

LIST OF ILLUSTRATIONS

LIST OF TABLES

CHAPTER 1

INTRODUCTION

Nanostructured materials have gained importance in recent years due to their significantly enhanced properties. The mechanical, magnetic and electrical properties exhibited by nanocrystalline materials are responsible for their usage in a number of advanced materials applications [1, 2, 3, 4]. Mechanical and electrical properties have been extensively studied but very little attention has been paid to their electrochemical (corrosion) behavior.

Corrosion is the destructive result of electrochemical reactions between a metal or alloy and its environment and is the primary means by which metals deteriorate [5]. A major cause for the premature failure of nickel and nickel alloys, stainless steel and aluminum alloys is a localized form of corrosion known as intergranular corrosion [5] which occurs due to chemical and structural non uniformities of grain boundaries. The grain boundary with enhanced free energy behaves like an anodic site and the interiors of the grains become the cathode resulting in intergranular corrosion.

Nanocrystalline metals have a large volume fraction of grain boundaries and a significant effect on corrosion is expected. On the other hand, a higher concentration of impurities is expected at the grain boundaries of microcrystalline metals compared to their nanocrystalline counterparts that possibly leads to more localized corrosion. Thus, the final corrosion behavior is expected to be influenced by these two opposing factors, i.e., grain boundary fraction and impurity level at grain boundaries. Some initial differences have been evident in the passive current density and open circuit potential of bulk and nano Ni. However, the electrochemical behavior of nanocrystalline nickel has not been established yet. Thus, it is essential to study the electrochemical (corrosion) behavior of nickel in various aqueous environments and develop an overall understanding.

This thesis is concerned with the study of corrosion behavior of bulk and nanocrystalline Nickel in 3.5% NaCl solution and 0.1N H_2SO_4.These two environments were selected to gain a better understanding of the corrosion behavior of nanocrystalline nickel, i.e., a pitting and a passivation environment.

Nanostructured nickel has been found to possess a number of enhanced mechanical and electrical properties in comparison to its bulk counterpart [6]. Thus, it has been an important material in a number of engineering components for space, biomedical and microelectromechanical (MEMS) devices. In the latter field, nickel is the material of choice over polysilicon as it possesses significant advantages. Nickel can be electroplated even at lower temperatures, unlike polysilicon which requires high temperature annealing that can cause damage to the electronic components already in place. MEMS devices, which are mainly produced by electroplating in small volumes are made of nanostructured micro components. One such application of nickel is in LIGA fabrication technology. The acronym LIGA comes from the German name for the process, ***L***ithographie*, **G**alvanoformung, **A**bformung* (LIGA).

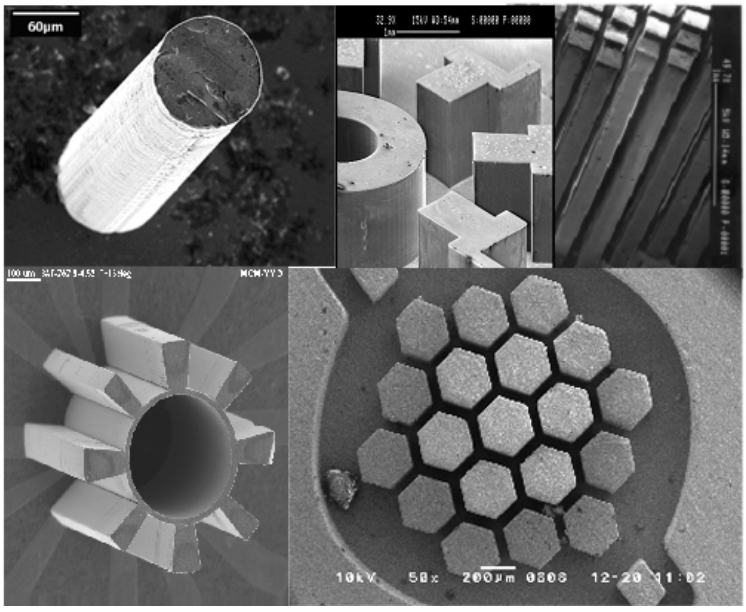

Figure 1.1 SEM micrograph of LIGA fabricated components.

LIGA uses lithography, electroplating and moulding processes to produce microstructures. The process [7] uses a special kind of lithography using X-rays to produce patterns in very thick layers of photoresist. The X-rays from a synchrotron are shone through a special mask onto a thick photoresist layer which covers a conductive substrate and the resist is then developed. The pattern formed is then electroplated with metal. In the electroplating step, nickel, (copper, or gold) is plated upward from the metalized substrate into the voids left by the removed photoresist. SEM micrograph of LIGA fabricated components is shown in Figure 1.1. Nickel electroplating is not only used in the chip industry but also for many other micro mechanical applications. Traditionally and presently most of the components that are susceptible to wear are plated from nickel.

CHAPTER 2

OBJECTIVE

Understanding the mechanisms of electrochemical passivation and localized corrosion at the nano scale is a challenging issue. Nanocrystalline materials have higher intercrystalline surface fraction that may lead to higher corrosion compared to their microcrystalline counterparts. This seems to be of particular importance to Nickel, the material of choice for LIGA MEMS components. Due to their small size, even a small corrosion attack at grain boundaries can lead to failure. On the other hand, a large density of grain boundaries present in nano Ni may distribute the corrosion action in a much larger area associated with grain boundaries and thus lead to a more uniform and lower intensity corrosion compared to its microcrystalline counterpart. It is evident that the above two counteracting factors (i.e., volume fraction of grain boundaries and uniformity of attack) will be important in determining the overall corrosion behavior of the attack.

Thus, the objective of the present study was to study the corrosion behavior of nano Ni in two entirely different environments, namely 3.5% NaCl solution and 0.1N H_2SO_4 and gain a better understanding of its corrosion behavior.

CHAPTER 3

BACKGROUND AND LITERATURE REVIEW

3.1 Nickel

Nickel is found in the first transition series of elements in the periodic table with the following properties: high melting point of 1453°C, forms an adherent oxide film, resists corrosion by alkalis, face-centered cubic (FCC) crystal structure, conferring ductility, forms alloys readily, both as solute and solvent, ferromagnetic at room temperature [8].

Nickel-based materials have a number of applications due to their special properties, Nickel iron alloys with low thermal expansion are used in clock pendulums, lead-frames in packaging electronic chips and in shadow-masks in television tubes storage and transportation tanks for the growing liquid natural gas industry. Due to their soft magnetic properties, they find applications in electronic devices and for electromagnetic shielding of computers and communication equipment. Equiatomic nickel-titanium shape memory alloys are used in actuators, hydraulic connectors and spectacle frames. Super elastic alloys are closely related materials that can undergo large elastic strains without plastic deformation. Medical devices and mobile telephone aerials are two applications in which this property is exploited [8].

Nickel electroplating is extremely well-known and widely applied. The technique has long been used to provide both corrosion-resistant and decorative finishes, and is also used to create the substrate for chromium coatings. Plating on plastics has enjoyed considerable growth recently. Nickel provides the corrosion resistance and lustrous appearance [8]. Nickel can also be deposited from solution without using electric current. These electroless nickel deposits are very uniform in thickness and contain phosphorus, which provides superior wear and corrosion resistance. The hardness can be increased by heat treatment, making these coatings well-suited to many pump and valve applications. A major application of electroless nickel today is in

computer hard discs. It forms an extremely uniform, smooth, stable, non-magnetic substrate for the magnetic recording layer, as well as providing corrosion protection for the underlying aluminum disc.

The estimated annual cost of corrosion in the U.S.A. alone is about $300 billion [8] -- equivalent to 4% of gross national product. The largest use of nickel alloys in in the area of corrosion prevention. Two thirds of all nickel produced goes into stainless steel to promote a stable, ductile, austenitic structure as well as contribute to corrosion resistance.

3.2 Nanostructured Materials

Nanostructured materials have captured much attention in the scientific community since their introduction in 1981 by Gleiter [1]. Nanostructure materials are materials with a microstructure the characteristic length of which is typically in the order of < 100 nm. The properties of nanostructured materials can be drastically different from those of single crystals or coarse grained polycrystals with the same average chemical composition. This deviation results from the reduced size or dimensionality of the nanometer sized crystallite and from the numerous interfaces between adjacent crystallites [1].

The unique properties of nanocrystalline materials are derived from their large number of grain boundaries compared to their coarse grained polycrystalline counterparts. In nanocrystalline solids, a large fraction of atoms (up to 49%) are boundary atoms [2]. Thus, the interface structure plays an important role in determining the physical and mechanical properties of nanocrystalline materials. As the size reduces into the nanometer range, the material exhibits peculiar and interesting mechanical and physical properties such as increased mechanical strength, enhanced diffusivity, higher specific heat and electrical resistivity compared to conventional coarse grained counterparts. Nanocrystalline metals have been found to exhibit creep and superplasticity with high strain rate at lower temperatures than their micro grained counterparts. High strain rate superplasticity at lower temperatures is of practical interest because it can offer an efficiently near-net-shape forming technique to industrial sectors.

Nanocrystalline materials exhibit higher yield strength and reduced tensile elongation compared to their microcrystalline counterparts. The hardness and yield strength tend to increase with decreasing grain size down to a critical value, as predicted by the well known Hall-Petch relationship. When the grain size is about 10 nm strength appears to decrease with further grain refinement. At this stage, dislocation sources inside the grain can hardly exist. This implies that dislocation pileups cannot form and the Hall-Petch relationship for conventional coarse grained materials is no longer valid. Instead, inverse Hall- Petch effect, i.e. softening is obtained when grain size is reduced [2].

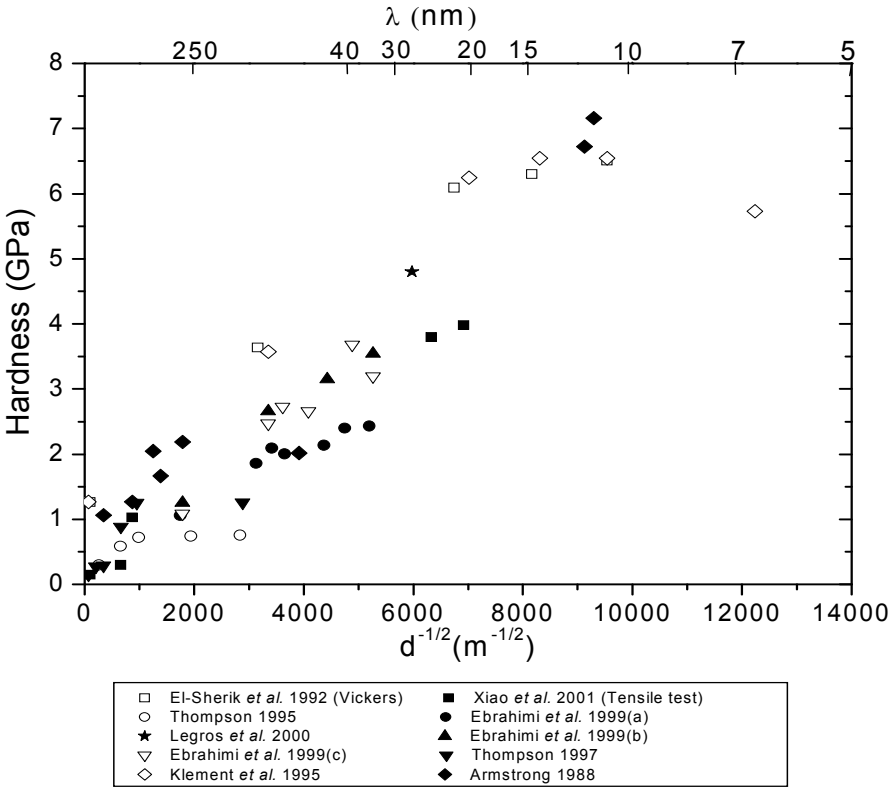

Figure 3.1 Summary of hardness data for nanocrystalline Ni [9].

Figure 3.1 summarizes several hardness measurements in nanocrystalline Ni. The data clearly indicates that a Hall-Petch relationship exists despite the various methods of preparation and sample characteristics. It has been found for nanocrystalline nickel, that a reduction in grain size <~ 10 nm produces a reduction in strength (inverse Hall-Petch effect). This transition has

been attributed to the effect of significant volume fraction of triple junctions. A grain size of ~7 nm has been determined as the upper limit of Hall-Petch relation where beneficial effects from reducing the grain size are attained [9].

As the mean grain size of a polycrystalline material is reduced to less than 100 nm, there is an overall increase in the volume fraction of atoms associated with the intercrystalline defects such as grain boundaries and tripe junctions in the material. Palumbo and co-workers [4] evaluated the grain size dependence of the intercrystalline volume fraction by assuming a three dimensional space filling fourteen sided tetrakaidecahedron as the grain shape where 14 sides represent grain boundaries and 36 edges the triple junctions, as shown in Figure 3.2. The resultant intercrystalline volume fraction of atoms, V_{ic} is given by,

$$V_{ic}=1-((D-\Delta)/D))^3 \quad (1)$$

where D is the mean grain size and Δ is the grain boundary thickness.

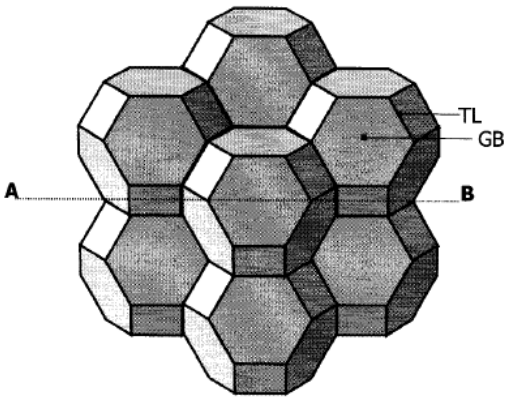

Figure 3.2 A stack of grains having tetrakaidecahedron topology packed in 3-d space where the 14 sides and 36 edges represent grain boundaries (GB) and triple lines (TL), respectively [4].

For electrodeposited nanocrystalline Ni, a High Resolution Transmission Electron Microscopy (HRTEM) study by Mehta et al. [10] revealed that the atomic arrangements at grain boundaries did not differ from those found in boundaries in conventional polycrystals. Kumar et al. [11] also observed clean atomically faceted grain boundaries in nanocrystalline Ni electrodeposits

identical to those in conventional polycrystalline Ni. Both studies have shown that the average grain boundary thickness in electrodeposited nano nickel is of the order of 1 nm.

Figure 3.3 presents a plot of intercrystalline volume fraction and grain size, illustrating the effect of grain size refinement from 10 μm to 4 nm on the calculated intercrystalline volume fractions according to equation 1, using nominal grain boundary thickness of 1 nm. Considering the lattice parameter for Ni, which is 0.352 nm [12] and grain boundary thickness of 1 nm, the grain boundary affected zone in nickel would span a distance of ~1.4 lattice parameters away from the grain boundary on either side. It can be seen from Figure 3.2 that the intercrystalline volume fraction becomes comparable to that of the crystalline volume fraction for solids with grain sizes <10 nm. The atoms at the intercrystalline region deviate from the perfect lattice sites in order to accommodate the misfit. Thus, at such a high intercrystalline volume fraction in a nanocrystalline material, a considerable portion of the atoms in the microstructure have different nearest neighbor coordination as schematically illustrated in Figure 3.4.

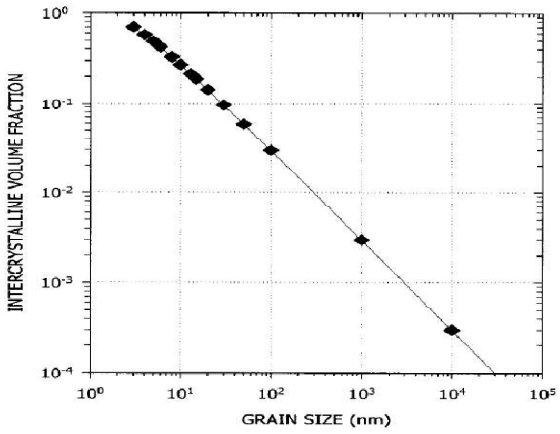

Figure 3.3 Calculated volume fraction of intercrystalline regions as a function of grain size based on the geometric model shown in Figure 3.2, assuming a grain boundary thickness of 1 nm [4].

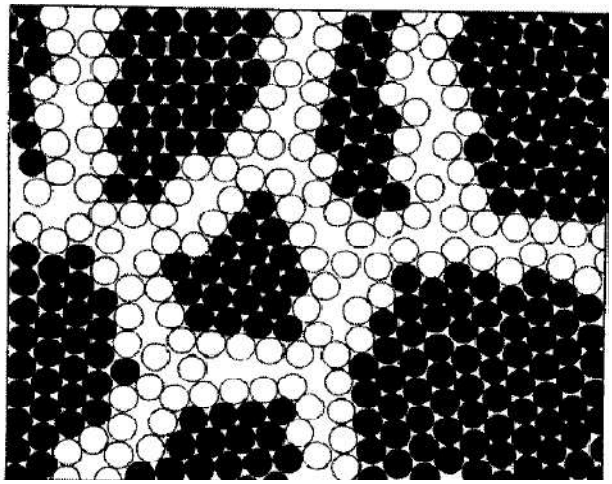

Figure 3.4 Two dimensional model of a nanocrystalline material comprising atoms in the grain interiors (●) and atoms in the intercrystalline core regions (o) [13].

3.3 Synthesis of Nanostructured Materials

The synthesis of nanomaterials involves (i) Materials and/or devices with reduced dimension and/or dimensionality in the form of nanometer sized particles, thin wires or thin films [2]. Some of the techniques used to generate this type of microstructure include chemical vapor deposition (CVD), physical vapor deposition (PVD), inert gas condensation, aerosol techniques, and precipitation from vapor from supersaturated liquids or solids. Examples are, catalysts and semiconductor devices utilizing single or multi layered quantum well structures.

(ii) Materials and/or devices in which the nanometer –sized microstructure is limited to a thin nanometer sized surface region of a bulk material, PVD, CVD, ion implantation and laser beam treatments are most widely applied procedures to modify chemical composition and/or atomic structure of solid surfaces on a nanometer scale. Surfaces with enhanced or protective coatings are examples. Also, included in this category are patterns in the form of an array of nanometer sized structural pattern on the free surface such as quantum dots synthesized by lithography.

(iii) Bulk solid with a nanometer scale microstructure, bulk solids in which chemical composition and the atomic arrangement of the crystallites or atomic/molecular groups forming

the solid vary on a length scale of a few nanometers throughout the bulk. Glasses, gels, supersaturated solid solutions or implanted materials are examples of this type.

Figure 3.5 represents a broad classification of nanomaterials and Table 3.1 shows the different mechanisms involved in nanomaterials processing with examples.

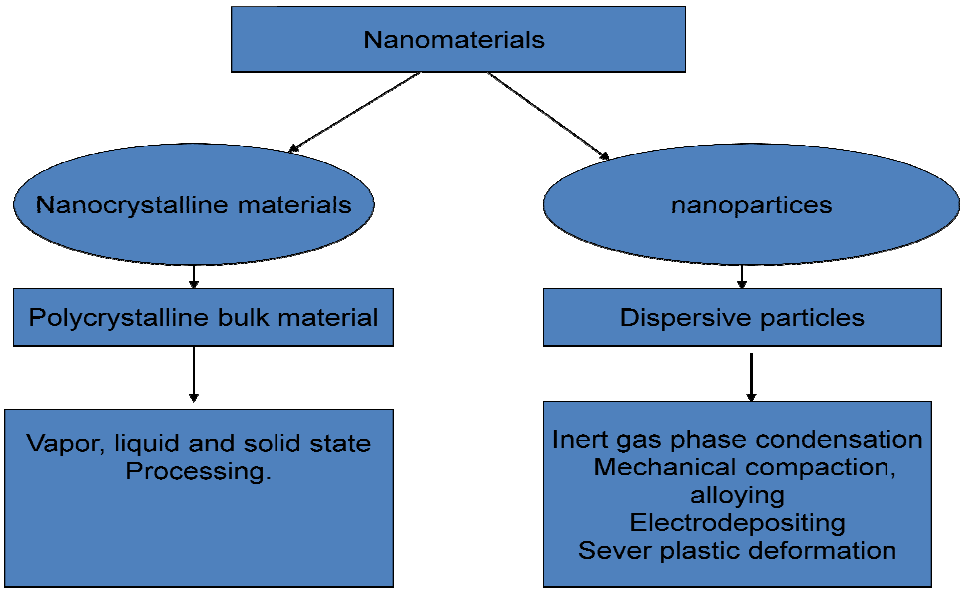

Figure 3.5 Flowchart representing classification of nanomaterials and their processing techniques [2].

Table 3.1 Different Mechanisms of Nanomaterials Processing along with Examples [3].

Vapor Phase Processing	**Liquid Phase Processing**	**Solid State Processing**	**Chemical Processing**	**Electrochemical Processing**
Inert gas condensation Sputtering CVD PVD	Rapid solidification Thermal Spray coating Solution Precipitation	Ball Milling Mechanical attrition Crystallization from amorphous precursors	Mixed alloy processing Sol gel processing	Electroless plating Electrodeposition

3.4 Production of Nanocrystalline Materials by Electrodeposition

The electrodeposition process for the production of nanocrystalline materials has many advantages over other alternative nanoprocessing techniques which include [13]

i. Rapidity, low cost, free from porosity, high purity, industrial applicability.

ii. Potential to overcome shape limitations or allows production of free standing parts with complex shapes, higher deposition rates, produce coatings on widely differing substrates.

iii. Ability to produce structural features with sizes ranging from nm to μm. Easy to control alloy composition, ability to produce compositions unattainable by other techniques.

iv. The possibility of forming simple low-cost multilayers in many different systems, Cu/Ni, Ni/Ni, Ni-P, etc and no post deposition treatment is required.

Many experimental measurements on physical, chemical and mechanical properties as a function of grain size in nanocrystalline materials produced by electrodeposition have demonstrated tremendous improvement [14, 15].

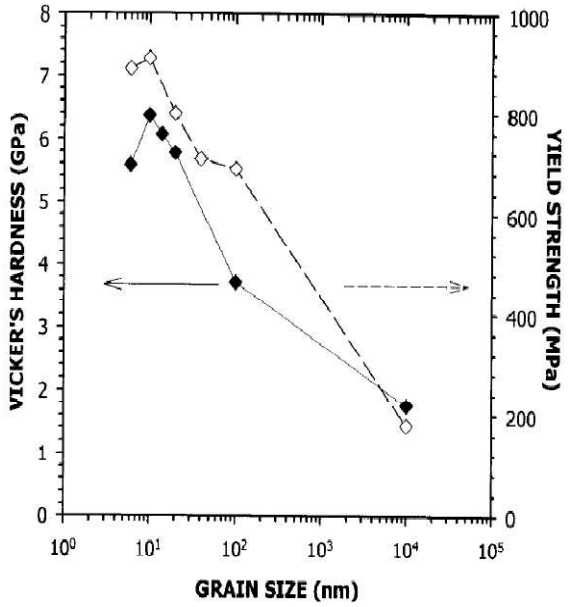

Figure 3.6 Plot indicates that the hardness and yield strength of nickel increased by a factor of 5 to 6 when the grain size was reduced from 10 μm to 10 nm [17].

Figure 3.6 represents some of the mechanical properties that are enhanced as a result of nanoprocessing for nickel. The hardness and yield strength of nickel increased by a factor of 5 to

6 when the grain size was reduced from 10 μm to 10 nm [16], the adhesive and abrasive resistance of nanocrystalline nickel electrodeposits improve also considerably [17, 18]. Table 3.2 presents a comparison of mechanical properties of conventional and nanocrystalline Ni [17].

Table 3.2 Comparison of Mechanical Properties of Conventional and Nanocrystalline Ni [6].

Property	**Ni (10 μm)**	**Ni (100 nm)**	**Ni (10 nm)**
Yield Strength, MPa (25^{o}C)	103	690	>900
Ultimate Tensile Strength, MPa (25^{o}C)	403	1100	>2000
Tensile Elongation, % (25C)	50	>15	1
Elongation in Bending % (25^{o}C)	-	>40	-
Modulus of Elasticity, GPa (25)	207	214	204
Work hardening Coefficient	0.4	0.15	0.0
Fatigue Strength ,MPa (10^{8} cycles/air/25C)	241	275	-
Wear Rate (dry air pin on disc) ($\mu m^{3}/\mu m$)	1330	-	7.9
Coefficient of Friction (dry air pin on disc)	0.9	-	0.5

All material properties such as heat capacity, thermal expansion, Young's Modulus and saturation magnetization are strongly dependent on grain size. These properties are little affected over a grain size range of 20 nm to 10 μm in the case of nickel. Some of these properties only begin to show grain size dependence at very small grain sizes less than 20 nm. For example, Zhou et al. [19] observed some reduction in Young's modulus for nickel samples having average grain sizes smaller than 20 nm.

3.5 Corrosion

Corrosion is the destructive action of an electrochemical reaction between a metallic component and its environment and is the primary means by which metals deteriorate [5]. The same amount of energy needed to extract metals from their minerals is emitted during the electrochemical reactions that produce corrosion. All corrosion processes involve transfer of

electronic charge in aqueous solutions, making it necessary to understand the electrochemical nature of corrosion.

Most metals corrode on contact with water (or moisture in the air), acids, bases, salts, oils, aggressive metal polishes, and other solid and liquid chemicals. Metals will also corrode when exposed to gaseous environments like acid vapors, formaldehyde gas, ammonia gas, and sulfur containing gases. Corrosion specifically refers to any process that causes “oxidation” or transforms metals from the “metallic” (zero valence) to the ionic form by removing electrons.

3.5.1 Pitting Corrosion

Polarization is the potential change from the equilibrium electrode potential caused by a net surface reaction [5]. For anodic polarization, electrons are removed from the metal, a deficiency results in positive potential shift due to the slow liberation of electrons by the surface reaction.

A condition of corrosion resistance due to formation of thin surface films under oxidizing conditions with high anodic polarization is known as passivity [5]. While this effect is in some sense a property of the material, it serves as an indirect kinetic barrier. The reaction is often quite rapid unless and until an impermeable layer forms. Localized attack in an otherwise resistant surface produces pitting corrosion. The pits may be deep, shallow or undercut. Pitting is a form of extremely localized corrosion that leads to the creation of small holes in the metal. The driving power for pitting corrosion is the depassivation of a small area, which becomes anodic while an unknown but potentially vast area becomes cathodic leading to very localized galvanic corrosion. The corrosion penetrates the mass of the metal, with limited diffusion of ions.

Figure 3.7 shows a schematic representation of corrosion behavior, indicating the possible variations of the anodic behavior of various metals in aqueous solutions [20]. When the potential is increased in the positive direction from the corrosion potential, E_{corr}, the current increases initially following a linear relation between the logarithm of the current and the potential until an approximately constant current is reached.

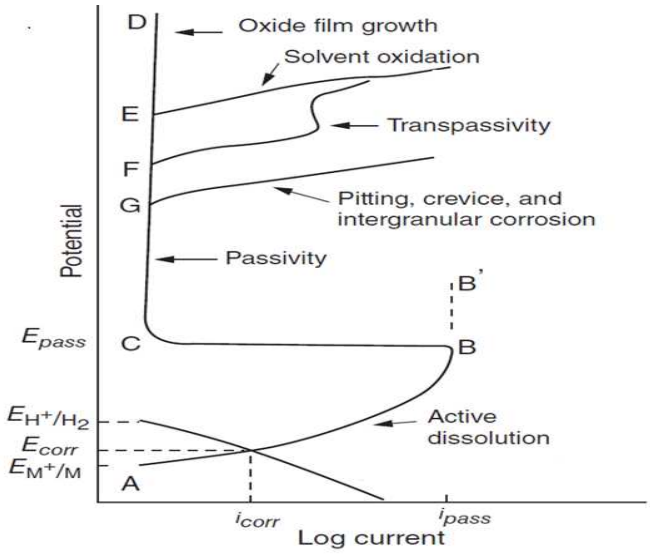

Figure 3.7 Variation of the anodic behavior of passivating metals in aqueous solutions [20].

The curve from E_{corr} to B indicates active dissolution of the metal. With further increase in potential, the current may remain high and constant (B to B') or decrease by several orders of magnitude (B to C) due to the formation of a thin oxide film (passive layer) . The corresponding potential is known as passivation potential E_{pass} (E_p) and the corresponding current is i_{pass} (I_p). On increasing the potential further, the thickness of the oxide film will increase but current in the range will essentially remain constant.

When the oxide film is a poor conductor of electricity, very high potential can be reached as shown in the curve from C to D. If the oxide film is a good electronic conductor (like nickel) a significant increase in current will occur at a certain potential (E) which in aqueous systems corresponds to the evolution of oxygen due to oxidation of water. If the oxide film is composed of cations which can be oxidized to higher oxidation state forming soluble products an increase in current may occur at lower anodic potentials (F) accompanied by the dissolution of metal due to transpassivity. In many metals and alloys which exhibit passive behavior, the passive film becomes locally unstable above a critical potential in solutions containing halide anions, particularly chloride. In Figure 3.7 a sudden increase in current is observed above G which corresponds to breakdown of passivity leading to various forms of localized corrosion.

Depending on the morphology, if a chemical micro or macro heterogeneity is developed at the metal/solution interface, it can be classified as pitting or crevice corrosion. If a chemical micro heterogeneity exists in the metal, selective dissolution or intergranular attack can occur.

The Pourbaix diagram, (potential/pH diagram) is a map [5] showing conditions of solution oxidizing potential and acidity or alkalinity for the various possible phases that are stable in an aqueous electrochemical system. Pourbaix diagrams show the reactions and reaction products that will be present when equilibrium has been attained, assuming all the appropriate reactions have been included. Thus, potential, pH in some cases can be adjusted to prevent corrosion thermodynamically. Although the Pourbaix diagram gives the stable phases for given conditions of potential and pH, other thermodynamically unstable phases formed in the past may still be present because they are slow to decompose. However, it should be noted that thermodynamics and the Pourbaix diagram do not provide any information on the rates of the reaction they describe.

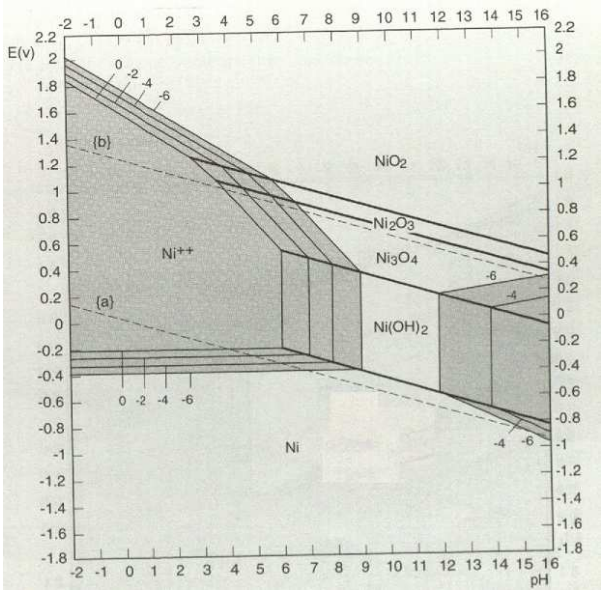

Figure 3.8 Representative Pourbaix diagram for Ni, Labels 0, -2,-4 and -6 are the log of soluble ion activity for the indicated lines [5].

The Pourbaix diagram for Ni is show in Figure 3.8. The Pourbaix diagram indicates that below a pH of 9 Ni has the potential to corrode. Since deionized water typically has a pH around 7, thermodynamically nickel can corrode in aerated water. Corrosion is possible in areas of the Pourbaix diagram where soluble ions of the metal are stable. The darker regions indicate areas of corrosion susceptibility. The metal is possibly resistant to corrosion or passive in areas where an oxide is stable. In areas where only the reduced form of the metal is stable, the metal is thermodynamically immune to corrosion.

3.6 Corrosion in Nanocrystalline Materials

Conventional metallic components are polycrystalline in nature and comprise of distinct crystals that are typically greater than 1 μm in size aggregated to form a solid. Grain boundaries, where differently oriented crystals meet are defective areas in the solid material with enhanced free energy compared with the crystal (grain) interiors. The grain boundaries are preferred sites for impurity segregation due to the increased average inter atomic spacing associated with them. A major cause for the premature failure of nickel and nickel alloys, stainless steel and aluminum alloys is a localized form of corrosion known as intergranular corrosion which occurs due to chemical and structural non uniformities of grain boundaries. The grain boundary with enhanced free energy behaves like an anodic site and the interiors of the grain become the cathode resulting in intergranular corrosion [3.] A schematic representation of this type of corrosion is shown in Figure 3.9.

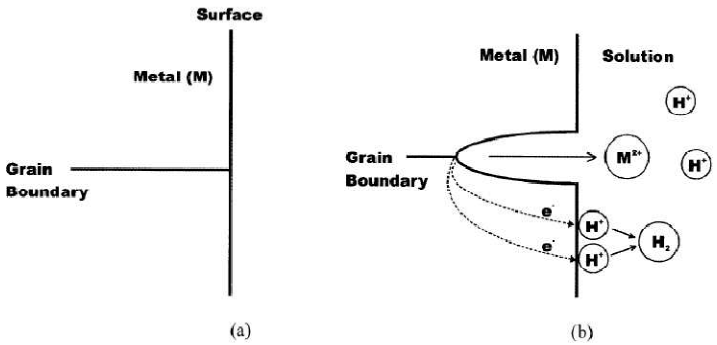

Figure 3.9 Schematic diagram showing (a) surface of a polycrystalline material before corrosion and (b) intergranular corrosion where the grain boundary and interiors act as anode and cathode, respectively [3].

Nanocrystalline metal surfaces contain significant densities of grain boundaries and triple junctions per unit area at the free surface. Wang [21] studied the grain size dependence of intercrystalline volume fraction to calculate intercrystalline surface fraction and the crystal/intercrystalline surface ratio, to correlate these factors with the corrosion behavior of nanocrystalline materials. Wang considered a 14 sided tetrakaidecahedron, and a cross section along the A-B plane (as shown in Figure 3.10) was considered to represent the interfacial regions emerging on an ideally flat free surface of a solid. From Figure 3.10, a is the length of the tetrakaidecahedron, D is the grain size of the crystal, Δ is the grain boundary width. From this crystallographic model, the surface fraction of the intercrystalline component S_{ic} as well as the crystal to intercrystalline area ratio ($S_c/_{Ic}$) was given by the following relationship

$$S_{ic} = 1 - (1-(\sqrt{3}\Delta/D))^2 \; ; \; Sc_{/ic} = ((1-S_{ic})/S_{ic}) \qquad (2)$$

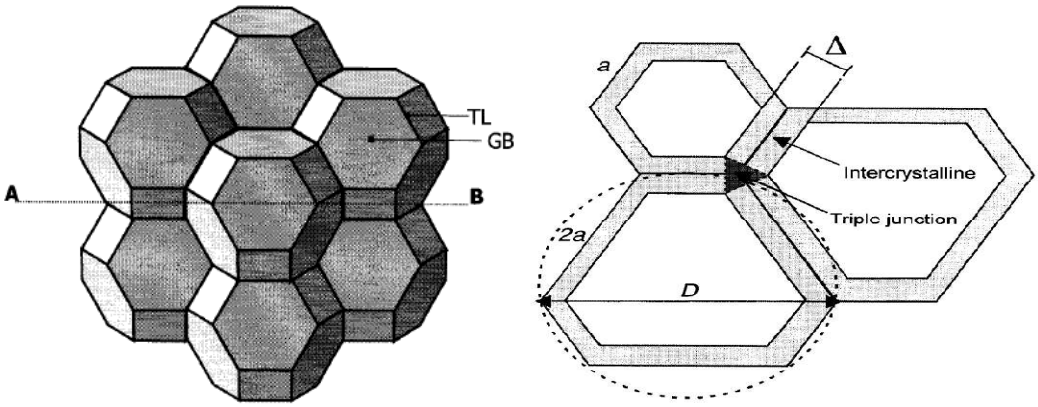

(a) (b)

Figure 3.10 (a) A stack of grains having tetrakaidecahedron topology packed in 3-d space where the 14 sides and 36 edges represent grain boundaries and triple lines respectively. (b) Schematic representation of the surface profile with the interfacial region on the free surface resulting from cross section along the plane A-B in (a), where a is the edge length and D is the grain size Δ is the grain boundary thickness [21].

From equation 2, a plot of intercrystalline surface area fraction and the surface area ratio of the crystal to the intercrystalline regions as a function of grain size in the range of 3 nm to 10 μm using a nominal grain boundary thickness of 1nm was plotted as shown in Figure 3.11. A

grain size reduction from 10 μm to 5 nm leads to an increase in the intercrystalline surface fraction from 0.03% to 55%. This is similar to the grain size dependence of the intercrystalline volume fraction considered by Palumbo and co-workers [4].

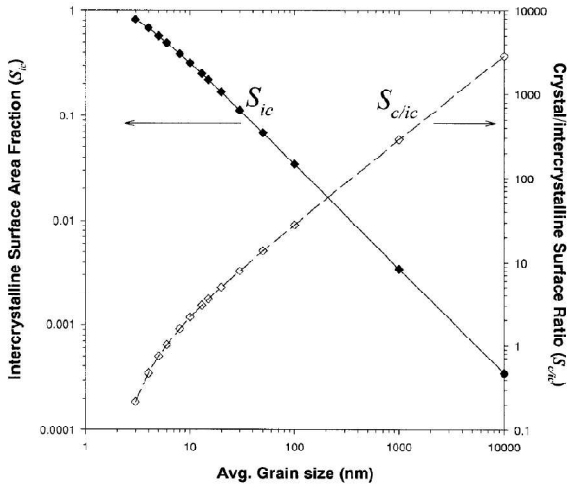

Figure 3.11 The effect of grain size on the calculated intercrystalline surface area fraction (S_{ic}) and the crystal/intercrystalline surface ratio ($S_{c/ic}$) assuming a grain boundary thickness of 1 nm [21].

Atoms at the intercrystalline region are in non equilibrium state and occupy higher energy states than corresponding atoms on a crystalline surface, assuming there are no surface reconstructions in either component. The enhanced intercrystalline surface fraction may increase the overall dissolution rate and result in a poor corrosion performance of nanocrystalline materials in an environment where formation of oxide films is excluded.

If the intercrystalline region is considered to be more anodic than the crystal region, the magnitude of the galvanic attack is associated with the relative areas of cathode (crystals) and anode (intercrystalline region) and their surface area ratios would influence the rate of galvanic corrosion. It can be seen from Figure 3.11 that this ratio has a strong dependence on grain size and it decreases by three orders of magnitude, approaching unity as the grain size decreases from 10 μm to approximately 5 nm. It is known from the basic principle of corrosion that a large ratio of cathode to anode surface area is to be avoided [5] as the preferential corrosion on the anode is concentrated on small areas which facilitates rapid penetration at the anode as often observed for polycrystalline materials. A schematic representation of anodic current density

distributions [21] for polycrystalline materials and nanocrystalline materials assuming grain interior and intercrystalline defective sites to be cathodes and anodes, respectively is shown in Figure 3.12.

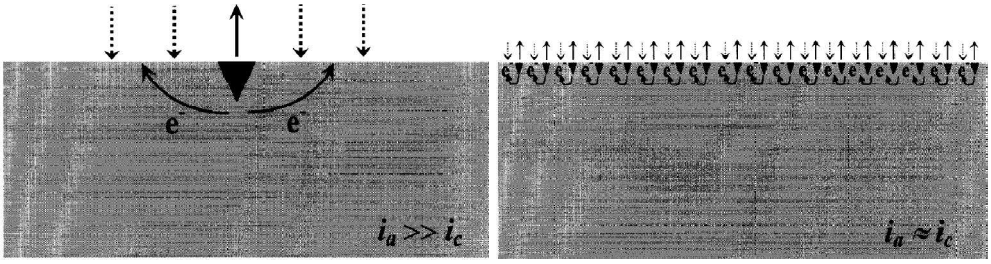

(a) (b)

Figure 3.12 Schematic representation of anodic current density distribution for (a) polycrystalline materials (b) nanocrystalline materials assuming grain interior and intercrystalline defective sites to be cathodes and anodes, respectively [20].

The effect of the decreased Sc/ic ratio on spreading the anodic current distribution and reducing the rate of penetration results in the nanocrystalline material to posses higher resistance against localized corrosion than their polycrystalline counterpart in systems in which solute segregation and precipitation of second phase particles at grain boundaries can be ignored.

3.6.1 Effect of Surface Defects on Passive Film Formation

Using X-ray photoelectron spectroscopy (XPS) Rofagha et al. [22] showed that the highly disordered surface on nanocrystalline Ni electrodeposits of grain size 50 and 32 nm leads to the formation of a more defective passive film in 1M H_2SO_4. This was correlated with the observed higher passive current densities relative to conventional polycrystalline Ni. In contrast, Zieger et al. [23], reported that a nanocrystalline $FeAl_8$ alloy of grain size 40 nm produced by sputtering was more easily passivated resulting in smaller passive current in 0.1M Na_2SO_4 at pH= 6. The higher passive film formation rate of the nanocrystalline structure was rationalized by the enhanced diffusion of passivating elements such as Cr along intercrystalline regions. This idea was based on oxidation studies by Merz and co-workers [24, 25] who found that the lower oxidation rate on a small grain size (4 μm) stainless steel sample was associated with the

enhanced grain boundary diffusion and selective oxidation of Cr forming a more effective Cr rich oxide relative to the coarse grain size stainless steel sample.

Szklarska et al. [26] found that nanocrystalline pure metals (Ni and Al) as well as binary alloys (Fe-Cr and Ni-Cr) showed lower passivation current densities and higher pitting potentials in solutions containing aggressive Cl^- anions. According to Szklarska et al. [26], at the nano grain size scale, the oxide film is more homogeneous due to the uniformity of distributed defects in the passive film. It was suggested that the accumulation of aggressive ions such as chloride ions in such shallow defects is more difficult and as a result would require higher driving force to penetrate the oxide film in comparison to a material with deeper defects such as expected in polycrystalline counterparts.

3.7 Corrosion Behavior of Nanocrystalline Nickel

The corrosion behavior of nanocrystalline materials produced by different methods has been studied for a variety of systems including pure metals, binary and ternary alloys and composites. There are three basic synthesis routes that have been applied to produce nanostructure materials for corrosion studies. Most of the early work (1975-90) dealt with materials produced by crystallization of amorphous precursor materials. The second group of materials that has been extensively studied since 1990 are nanostructures produced by electrodeposition and materials produced by sputter deposition has been studied since about 1992.

Rofagha et al. [27, 28] first investigated the corrosion behavior of nanocrystalline Ni electrodeposits in 2N H_2SO_4 (pH=0) using potentiostatic and potentiodynamic polarization tests. Nanocrystalline electrodeposits of grain sizes 500, 50 and 32 nm were used and they exhibited similar active, passive and transpassive behavior as conventional polycrystalline Ni (grain size of 100 μm) with about one order of magnitude higher passive current densities, Figure 3.13. The results showed that the higher passive current densities were due to a more defective (presence of higher number of grain boundaries, triple junctions) and passive film formed on the highly disordered nanocrystalline Ni surfaces [21]. There was a positive shift of -200 mV in the corrosion

potential for the nanocrystalline samples which was thought to be the result of the catalysis of hydrogen evolution reaction. More uniform corrosion morphology was observed for the nanocrystalline Ni after considerable metal dissolution by potentiostatic testing at 1.2 V (SCE) for 2000 seconds in 1M H_2SO_4.

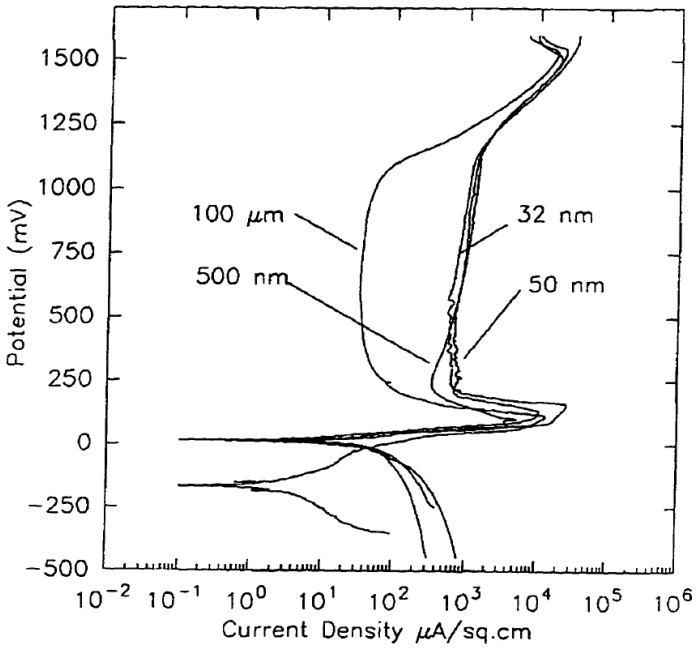

Figure 3.13 Potentiodynamic polarization curves of nanocrystalline and microcrystalline Ni in 2N H_2SO_4 at ambient temperature [28].

El-Sherik and Erb [29] studied the corrosion behavior of nanocrystalline Ni by exposing the material to a salt spray environment (ASTM B-117). In this study, both nanocrystalline and conventional Ni electroplated as coatings (thickness 10 μm) on to mild steel substrate were compared. The nanocrystalline Ni provided the same protection against corrosion of steel substrate as conventional microcrystalline electrodeposits. Figure 3.14 presents the salt spray test results for bare mild steel and mild steel coated with nanocrystalline and microcrystalline Ni.

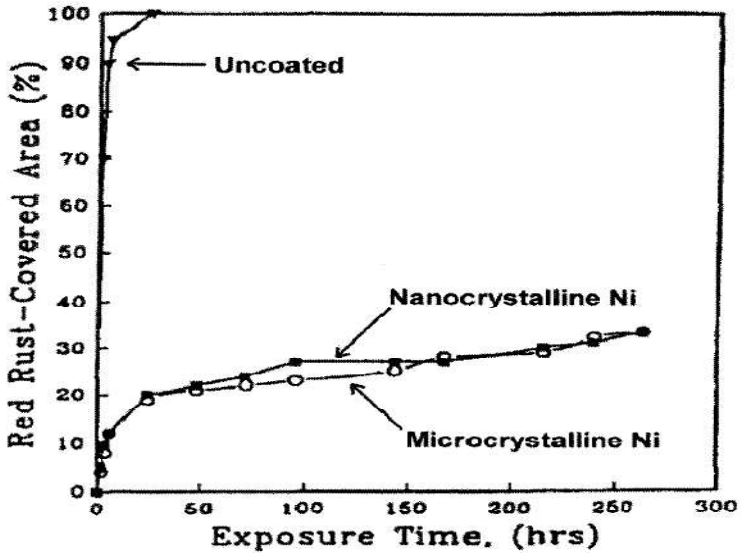

Figure 3.14 Salt spray test results for bare mild steel and mild steel coated with nanocrystalline and microcrystalline Ni [29].

Tang et al. [30] compared the corrosion performance of nanocrystalline Ni electrodeposits having grain size 5-10 nm prepared using various plating techniques such as direct current plating, pulse current by immersing test coupons in various acids (7M nitric acid, 3M hydrochloric acid and 20 gdm^{-3} citric acid solutions) as well as exposure to moist SO_2 environment. Considerable differences in the corrosion resistance were found among the differently synthesized specimens and the results were interpreted in terms of distinct changes in crystallographic texture observed in these materials.

Wang et al. [31] investigated the corrosion behavior of electrodeposited nanocrystalline Ni (grain size 16 nm and 32 nm) in 30% KOH (pH=14.8). It was found that microcrystalline and nanocrystalline Ni readily passivated without showing a clear active passive region and the dissolution current densities in the passive region for nanocrystalline Ni samples were slightly higher (Figure 3.15). It was concluded that the current difference was not significant especially at high anodic potentials where conventional micro crystalline Ni was more susceptible to localized corrosion.

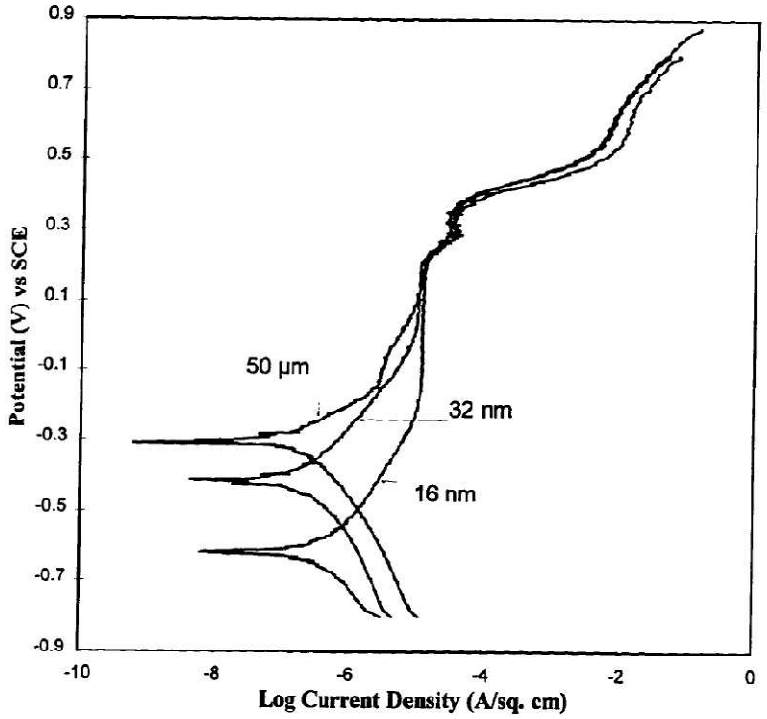

Figure 3.15 Potentiodynamic polarization curves for nanocrystalline and microcrystalline Ni in deaerated solution of 30% KOH at 24°C [31].

Corrosion studies were also conducted in 3 wt% NaCl (grain size of 30 nm, 17 nm and 100 µm) [31]. Figure 3.16 presents the potentiodynamic polarization behavior of the nano and microcrystalline Ni electrodes. The scans were run from -0.8 V to 0.8 V with respect to saturated calomel electrode (SCE), at a scan rate of 5 mVs^{-1}. At a potential of around 0.6 V (SCE), the passivation is suddenly deactivated. According to the Pourbaix diagram for the system, this may be due to the oxidation of the nickel oxide layer to a higher valence. The morphologies observed on the sample agreed with the explanation that corrosion is concentrated at grain boundaries and triple junctions. The microcrystalline sample which has larger grains proportionally has few atoms located at the triple junctions and grain boundaries. With a decrease in grain size the number of triple junctions increases which results in the increase in number of pits but a decrease in size of the pits. The pits in the nanocrystal sample become small and numerous and attack the surface uniformly.

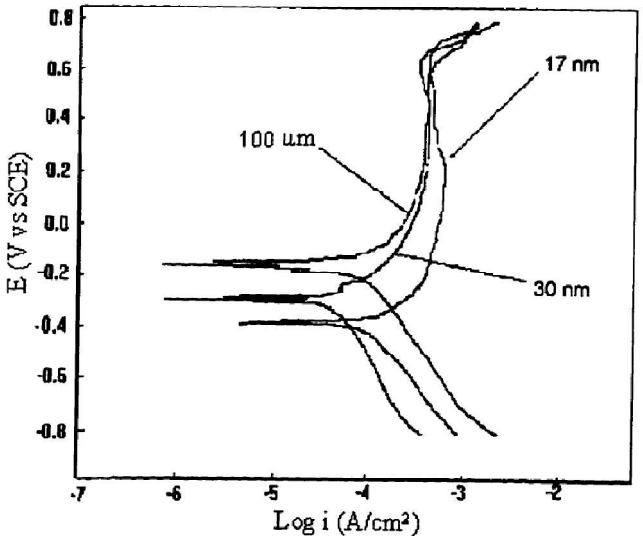

Figure 3.16 Potentiodynamic polarization curves of nanocrystalline and microcrystalline Ni in 3 wt% NaCl solution at ambient temperature with a scan rate of 5 $mVsec^{-1}$ [31].

It can be summarized from the above findings that intercrystalline corrosion in Ni is primarily due to passive film instability at grain boundaries. The difference in electrochemical behavior noted with nanocrystalline and microcrystalline Ni diminish only at potentials below the primary passivation potential (active dissolution) and above 1250 mV where general transpassive dissolution is expected. Nanocrystalline processing of Ni may catalyze the hydrogen reduction process, reduce kinetics of passivation and compromise passive film stability. This behavior is considered to be consistent with substantial contributions to the bulk electrochemical behavior from the intercrystalline regions of these materials leading to the development of protective Ni coatings. Nickel nanocrystalline specimens exhibit similar active – passive – transpassive behavior, typical of conventional Ni. Differences are evident in the passive current density and open circuit potential.

In acidic solutions, nanocrystalline Ni show higher current density in passive region resulting in higher corrosion rate. Higher current density is attributed to higher grain boundary and tripe junction content in nanocrystalline specimens. The positive shift in open circuit potential for nanocrystalline material is thought to be the result of catalysis of hydrogen evolution reaction. Nanocrystalline materials in general have been shown to have unique catalytic characteristics

which are the result of high defect content in the form of interfaces and triple junctions. The higher defective film on the nanocrystalline specimen allows for a more uniform breakdown of the passive film which in turn leads to a more uniform corrosion. In coarse grained nickel, the breakdown of the passive film occurs first at grain boundaries and triple junctions rather than at crystal surface leading to preferential attack at these defects.

The general progressive shift in the open circuit potential towards noble direction for the finer grain size deposits compared to bulk nickel is due to the predominance of hydrogen evolution reaction. Defects like dislocation affect the kinetics of hydrogen evolution reaction. Moreover, reversible trapping of hydrogen at dislocations, grain boundaries and voids can change kinetics of hydrogen evolution. Therefore, catalysis of hydrogen reduction process by substantial quantity of crystalline defects at the surface of Ni deposits during electrochemical testing shifts the open circuit potential value in a more noble direction.

For a polycrystalline specimen having large grains with proportionally small number of atoms located at triple junctions or grain boundaries, in alkaline solutions corrosion is concentrated at triple junctions and grain boundaries. Corrosion when localized at these sparse locations tends to result in large deep pits. As the grain size decreases the number of triple junctions and grain boundaries increases. Hence, the number of pits increases while their size tends to decrease. The same amount of nickel dissolves into solution but corrosion is more evenly distributed.

Critical current density of passivation for all Ni microstructures is found to be approximately similar indicating that the mechanism of onset of passivity and passivation itself is similar in nature for all nickel microstructures.

CHAPTER 4

EXPERIMENTAL

4.1 Material and Sample Preparation

4.1.1 Bulk Ni

Nickel 200, which is commercially pure (99.6%) wrought Ni was used as the bulk material. The bulk Ni used for electrochemical testing was epoxy mounted in the following manner:

Type 1: Discs of 3.6 cm in diameter were machined out from the as received Nickel 200 rod of diameter 3.81 cm. The discs were further machined to four equivalent parts of area 2.5 cm^2 and thickness of about 0.5 cm. Two of these discs were epoxy mounted for electrochemical testing.

Type 2: A rectangular piece of dimensions 21 mm x 25 mm was machined from the as received Nickel 200 rod. This was further cut into four equivalent parts of area 1.1 cm^2. The two parts were epoxy mounted on an aluminum stub of diameter 1.5 cm (using silver paste, for electrical contact) for electrochemical testing. A hole was drilled and taped into the aluminum stubs in order to provide electrical contact to the Ni specimen.

All electrode surfaces were mechanically polished with successively finer grades of silicon carbide sandpaper polishing down to grit of 1000 as the final step. Rinsed thoroughly with de ionized water and methanol being the final step. Miccrostop stop-off lacquer was used to prevent any leakage of the electrolyte into the working electrode set up.

4.1.2 Nano Ni

The electrodeposited nanocrystalline pure Ni materials used for experimental purpose were acquired from Integran Technologies Inc. The materials have full density (pore free) and a

narrow grain size range which has been achieved by the precise control of electrical and chemical parameters [32].The thickness of the material is 0.3-0.6 mm. Small sections, 1.2 mm x 0.5 mm and 1.2 mm x 0.4 mm of the Nano Ni were exposed for electrochemical testing, the rest of the area was sealed using miccrostop stop-off lacquer.

4.2 Electrochemical Cell

Figure 4.1 shows the K0047 Corrosion Cell from Princeton Applied Research [32] which is ideal for testing and evaluation of metal specimens in aqueous environments. It is fashioned after a well known cell configuration and is a standard in many ASTM methods.

The cell permits a series of metal specimens and liquid environments to be tested quickly and uniformly. Most of the common electrochemical techniques for corrosion testing can be employed under aggressive conditions (except for HF) and at ambient or elevated temperatures. This cell set up was used for all potentiostatic and potentiodynamic electrochemical testing.

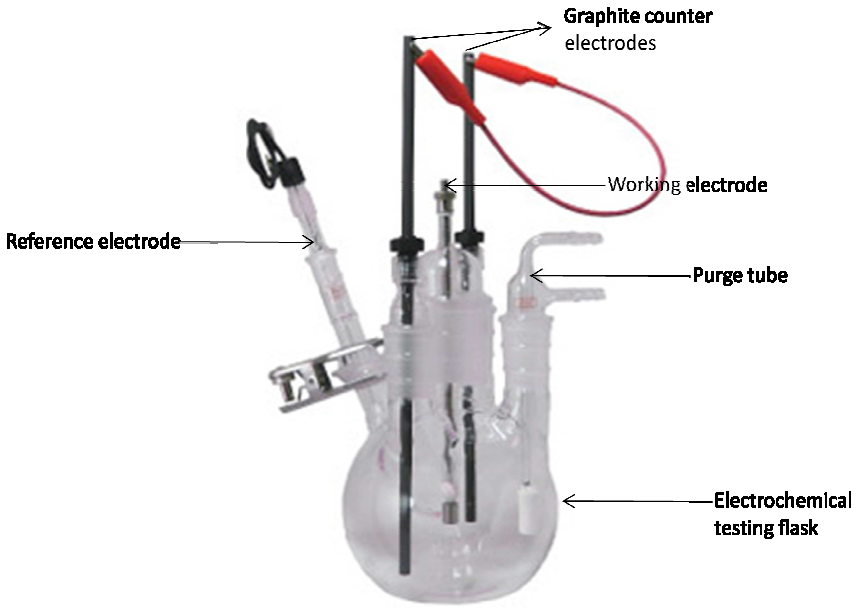

Figure 4.1 K0047 Corrosion Cell set up from Princeton Applied Research

4.3 Electrochemical Testing

All current-potential experiments were performed using an EG&G Princeton Applied Research Potentiostat/Galvanostat model 273A interface which was linked to a DELL compatible personal computer. The electrochemical data acquisition and analysis were conducted and automated with the software 352 SoftCorr III corrosion measurement software developed by Princeton Applied Research.

Figure 4.2 schematically illustrates the laboratory set up for polarization studies for the polycrystalline and nano crystalline specimens. CE, RE, WE represent the counter electrode, reference electrode and working electrode, respectively. The electrolytes used for testing were 0.1N H_2SO_4 and 3.5% NaCl, prepared in analytical grade de-ionized water. Saturated calomel electrode (SCE) was used as the reference electrode for all electrochemical experiments

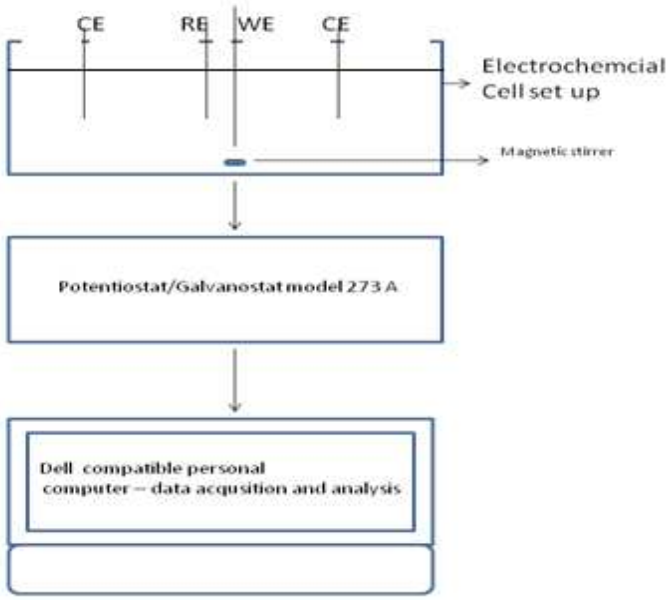

Figure 4.2 Laboratory set up for polarization studies for the bulk and nanocrystalline Ni. CE, RE, WE represent the counter electrode, reference electrode and working electrode, respectively.

4.3.1 Potentiodynamic Polarization Testing

Potentiodynamic polarization tests were performed in 0.1N H_2SO_4 and 3.5% NaCl aqueous solutions. The tests were conducted under aerated and deaerated conditions. The anodic polarization tests were initiated at 200 mV below the open circuit potential (OCP) and progressed to about 800 mV above OCP at a scan rate of 1 mVs^{-1}. All the deaeration tests were performed by purging argon gas for twenty minutes before starting the scan and continuing purging during the testing.

Potentiodynamic polarization tests on the electrodeposited nanostructured samples were also conducted with similar operating parameters and conditions. Following testing, potential vs current density plots were obtained by normalizing the current over the specimen surface area. A Tafel extrapolation method was used to calculate the corrosion rate.

4.3.2 Corrosion Potential vs Time Measurements

The equilibrium potential attained by the metal surface in the absence of electrical connections is the OCP. A stable value of E_{ocp} (open circuit potential) is taken to indicate that the system being studied has reached "steady state", i.e., the various corrosion reactions have assumed a constant equilibrium rate. Some corrosion reactions reach steady state in a few minutes, while others may need several hours. All open circuit potential *vs* time experiments were conducted until the potential stabilized. All potential-time tests were conducted in aerated conditions.

4.4 Materials Characterization

4.4.1 X-ray Diffraction

The grain size of the bulk and nano Ni was determined from the calculation based on the broadening of the X-ray diffraction (XRD) peak. The lowest 2θ angle diffraction peak was chosen for the calculations. The X-ray diffraction measurement was performed on a D-500 instrument. The X-ray source was Cu K_α (λ=1.542 Å). The X-ray diffraction analysis was performed for a scan from θ to 2θ value of 90 radians, at a step time of 0.1 for 26.42 minutes with a dwell time of 2.0. The crystalline grain size, d was estimated from the Scherrer equation [11],

$$d=(0.9\lambda\sqrt{(B^2-b^2)})/\cos\theta \quad (3)$$

where θ is half of the reported peak centroid, B is the reported peak full width at half maximum (FWHM) in radians, b the instrument's broadening and λ is the wavelength of the x-rays.

4.4.2 Scanning Electron Microscopy (SEM) and Energy Dispersive Electron Spectroscopy(EDS)

SEM in conjunction with EDS were conducted in order to study and analyze the surface morphology of the electrochemically tested bulk and nanocrystalline samples and to determine the composition and presence of other trace elements or impurities in the bulk and nanocrystalline samples. A Hitachi S-3000N variable pressure SEM with a resolution of 3.0 nm was used for the analysis. In this study, the SEM-EDS system was used at 20 kV acceleration voltage and working distance varied from 12 cm to 20 cm. Scanning electron micrographs were obtained at different magnifications in order to study surface features present after testing. EDS spectra were taken for the bulk and the nanocrystalline Ni prior to electrochemical testing.

4.4.3 Optical Profilometry

A Veeco Wyko NT9100 optical profiler was used to analyze the surface morphology and determine the depth profile of the pits formed in bulk and nano Ni after potentiodynamic polarization testing in 3.5% NaCl solution. The Wyko NT9100 Optical Profile employs coherence scanning interferometry, also known as white-light interferometry, white-light confocal, or vertical scanning interferometry to produce high quality three-dimensional surface maps of the object under examination.

CHAPTER 5

RESULTS AND DISCUSSION

5.1 XRD and EDS Characterization of Bulk and Nanocrystalline Nickel

Figures 5.1 (a) and (b) present the X-ray diffractograms of bulk and nanocrystalline Ni. Both types of Ni exhibit strong (111) and (200) diffraction peaks at 2θ values of 44.5˚ and 52.1˚, respectively. The (220) diffraction peak is not present in the nano Ni more likely because electrodeposition resulted in (111) and (200) growth. Both types of Ni show similar (111) / ((200) intensity ratios. The average grain size of the bulk Ni 200 was found to be about 41 μm [9]. The crystalline grain size d of the nano Ni, was estimated from the Scherrer equation [11],

$d = (0.9\lambda\sqrt{(B^2 - b^2)})/\cos\theta$

where θ is half of the reported peak centroid, B is the reported peak FWHM as shown in Figure 5.1 (c) , b is the instrument's broadening and λ is the wavelength of the X-rays. The (111) diffraction peak was used for grain size calculation. Grain size of nano Ni was found to be around 21 nm.

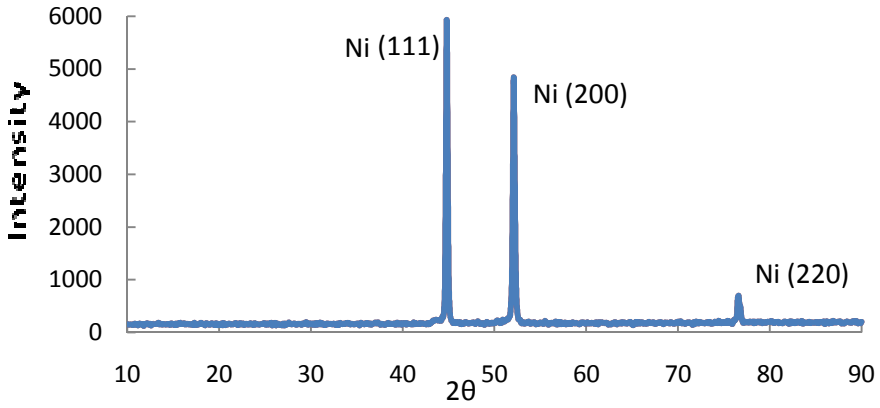

(a)

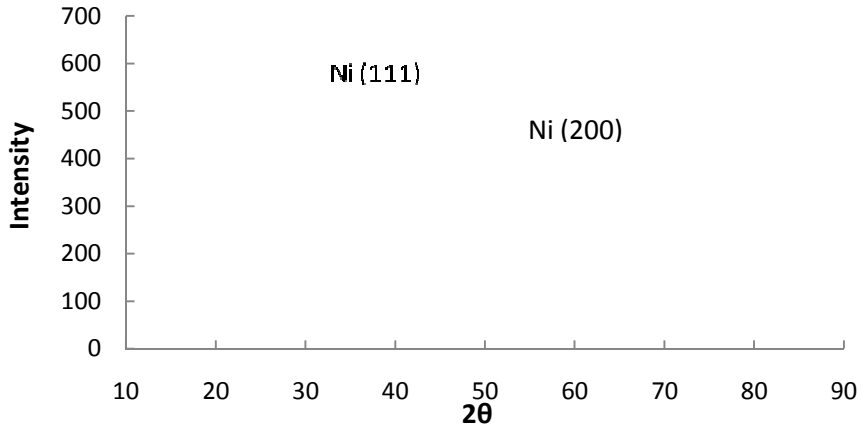

(b)

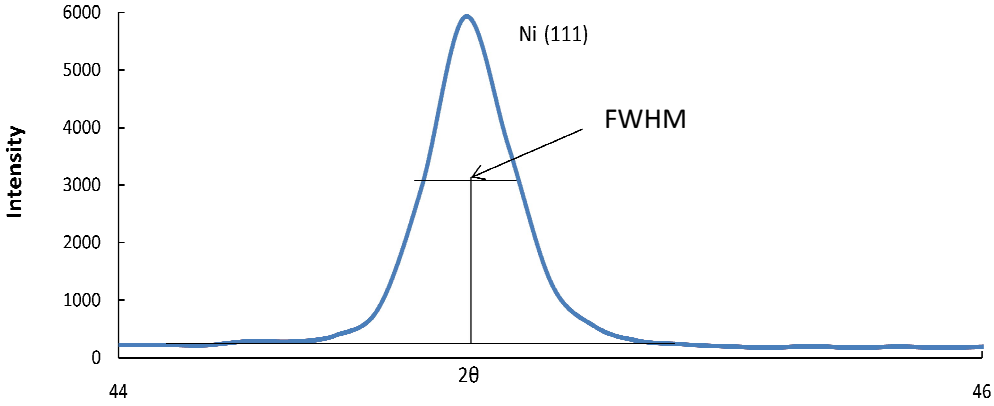

(c)

Figure 5.1 X-ray diffractogram of (a) bulk Ni and (b) nano Ni. (c) FWHM of the Ni (111) peak used for grain size calculation.

Figures 5.2 (a) and (b) present the EDS spectra for bulk and nano Ni, respectively. The analysis showed that both materials were mainly Ni with minor presence of C and O contaminants. Such contaminants are typically observed. Table 5.1 presents the weight percentage of Ni in bulk and nano Ni, along with the weight percentage of contaminants.

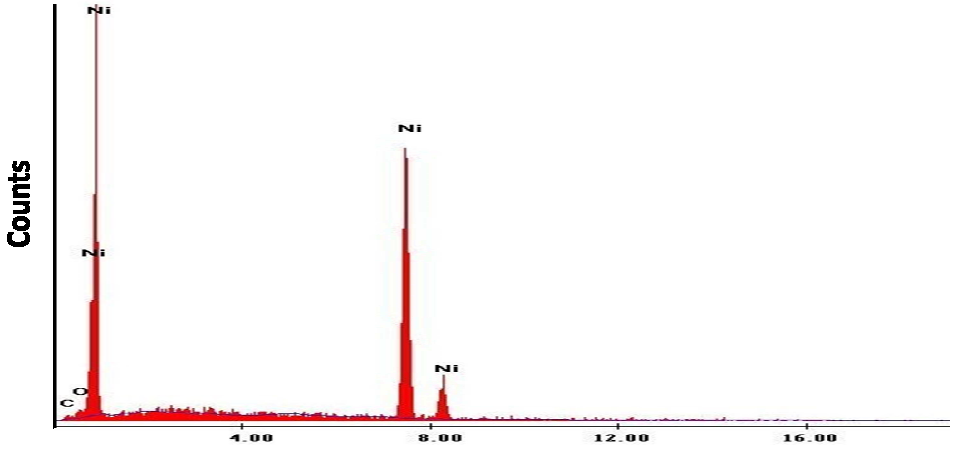

(a)

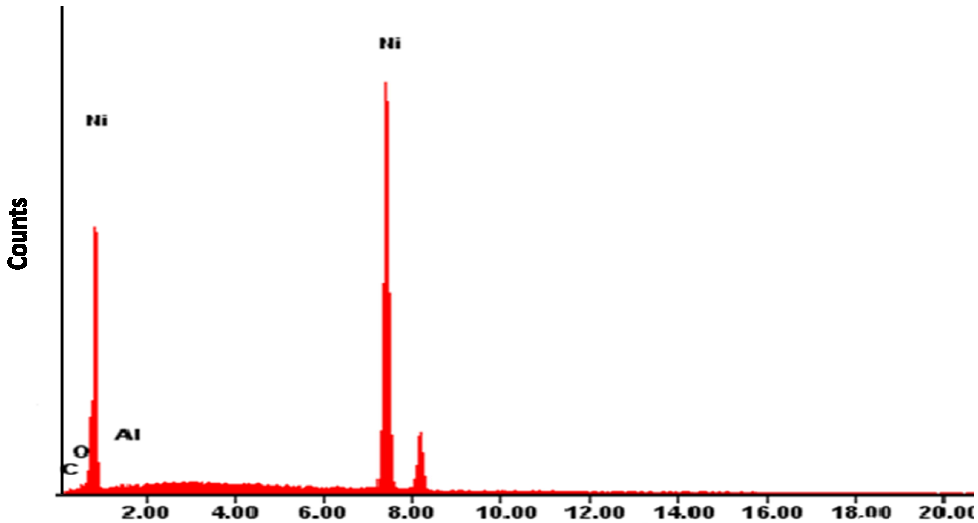

(b)

Figure 5.2 EDS spectra for (a) bulk and (b) nano Ni, respectively.

Table 5.1 Weight percentage of Ni and surface contaminants in bulk and nano Ni.

% Wt	Ni	C	O	Al
Bulk Ni	94.29	04.55	1.16	-
Nano Ni	93.88	04.28	1.31	0.53

5.2 Corrosion Behavior of Bulk Nickel

5.2.1 Potentiodynamic Polarization Response in 3.5% NaCl Solution

Potentiodynamic polarization tests were performed in 3.5% NaCl aerated and deaerated solution. The electrochemical cell and electrode assembly was arranged as described earlier in the experimental chapter. Figure 5.3 presents the anodic polarization curves for bulk Ni in 3.5% NaCl aerated solution. The general shape of the curve follows mainly activation polarization as seen in previous studies. The tests were conducted in this environment with excellent repeatability as evident from Figure 5.3.

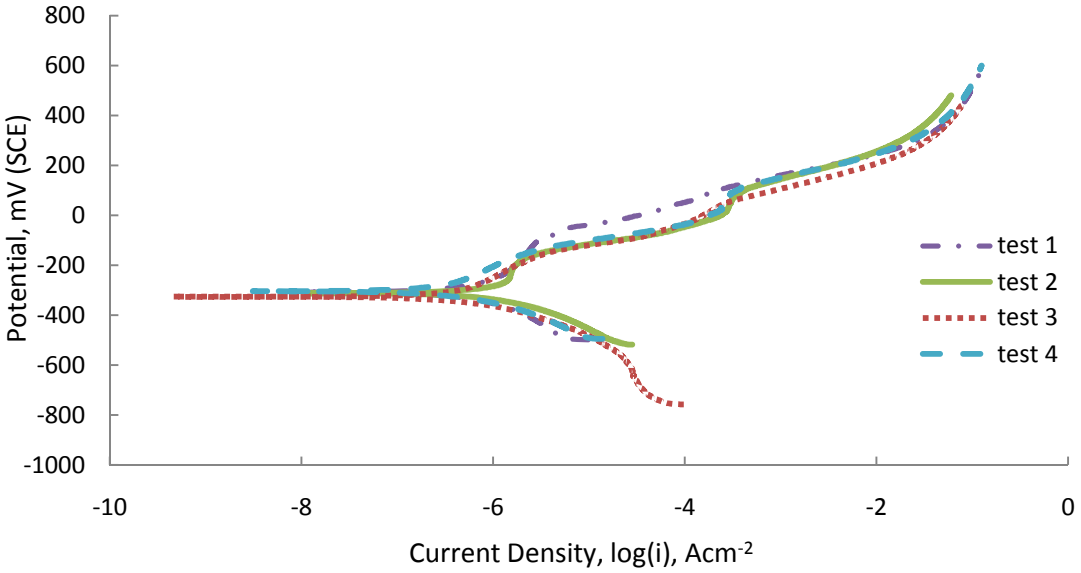

Figure 5.3 Potentiodynamic polarization behavior of bulk Ni in 3.5% NaCl aerated solution.

Polarization [5] is the potential change from the equilibrium half-cell electrode potential caused by a net surface reaction for the half-cell reaction. During anodic polarization, electrons

are removed from the metal and a deficiency results in positive potential shift due to the slow liberation of electrons by the surface reaction. Current density rather than current is proportional to corrosion rate because the same current is concentrated into a smaller surface area results in large corrosion rate. Corrosion rate is inversely proportional to area for the same dissolving current [5].

The anodic reaction in this case is

$$Ni \longrightarrow Ni^{2+} + 2e^{-} \quad (4)$$

The cathodic reaction for the reduction of dissolved oxygen in a neutral solution (pH=7) is

$$O_2 + 2H_2O + 4e^{-} \longrightarrow 4OH^{-} \quad (5)$$

Standard reduction potential, E° = +0.82 V *vs* Standard Hydrogen Electrode(SHE)

In a deaerated environment, the cathodic reaction becomes,

$$2H_2O + 2e^{-} \longrightarrow H_2 + 2OH^{-} \quad (6)$$

Standard reduction potential, E° = -0.413 V *vs* SHE

Table 5.2 presents the corrosion potential and corrosion rate as calculated from the anodic polarization experiments in the aerated environment. The average potential is about -312 mV and the corresponding average current density is found to be 1.12 μAcm^{-2}. The corrosion rate is very low indicative of the high corrosion resistance of Ni.

Table 5.2 Potentiodynamic polarization test results of bulk Ni in 3.5% aerated NaCl solution.

Parameter	test 1	test 2	test 3	test 4	Average Value ±SD
Corrosion Potential (mV)	-311.5	-325.3	-307.3	-302.1	-311.5 ±8.6
Corrosion Rate ($\mu A.cm^{-2}$)	1.68	1.14	0.89	0.75	1.12 ±0.37

SD: standard deviation

Figure 5.4 presents the anodic polarization response obtained for bulk Ni in 3.5% NaCl deaerated solution. It follows an activation behavior similar to that of bulk Ni in aerated

environment. Due to the absence of oxygen, in the deaerated environment, there is a drop in the corrosion potential and corrosion rate values. Table 5.3 presents the average corrosion potential and corrosion rate as calculated from the polarization curves. Bulk Ni exhibits a corrosion potential of -553 mV (SCE) and a corrosion rate of 0.28 μAcm^{-2}.

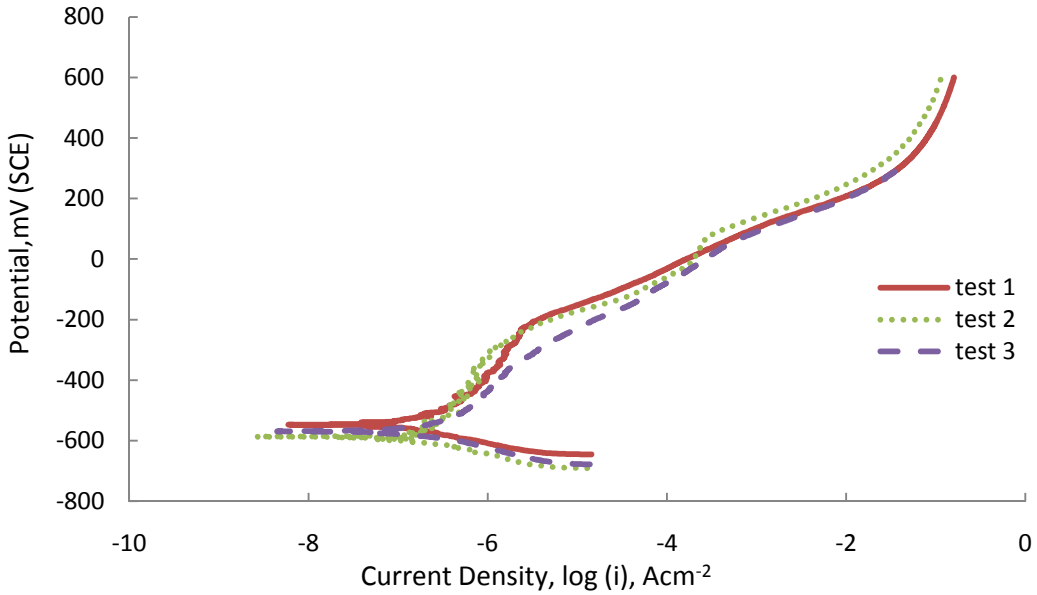

Figure 5.4 Potentiodynamic polarization behavior of bulk Ni in 3.5% NaCl deaerated solution.

Table 5.3 Potentiodynamic polarization test results of bulk Ni in 3.5% NaCl deaerated solution.

Parameter	test 1	test 2	test 3	Average Value ±SD
Corrosion Potential (mV)	-546.6	-558.9	-553.9	-553.1 ±6.0
Corrosion Rate ($\mu A.cm^{-2}$)	0.34	0.26	0.22	0.28 ±0.01

The polarization behavior of bulk Ni in these two environments can be compared by constructing an Evan's diagram (potential *vs* current density). Figure 5.5 graphically represents the behavior of bulk Ni in 3.5% NaCl aerated and deaerated solution. The anodic and cathodic reactions mentioned earlier are shown schematically on the graph. E_{corr} and E'_{corr} is the aerated

and deaerated corrosion potential respectively, with I_{corr} and I'_{corr} being the corresponding corrosion current density. E_{corr} is higher due to the presence of oxygen that increases the corrosion potential. As seen from Table 5.3, the average corrosion potential in the deaerated solution was found to be about -553 mV which is close to a potential difference of 200 mV below the aerated environment. As shown, the higher corrosion potential of the latter solution caused a fourfold increase in the corrosion rate (from 0.28 to 1.12 μAcm^{-2})

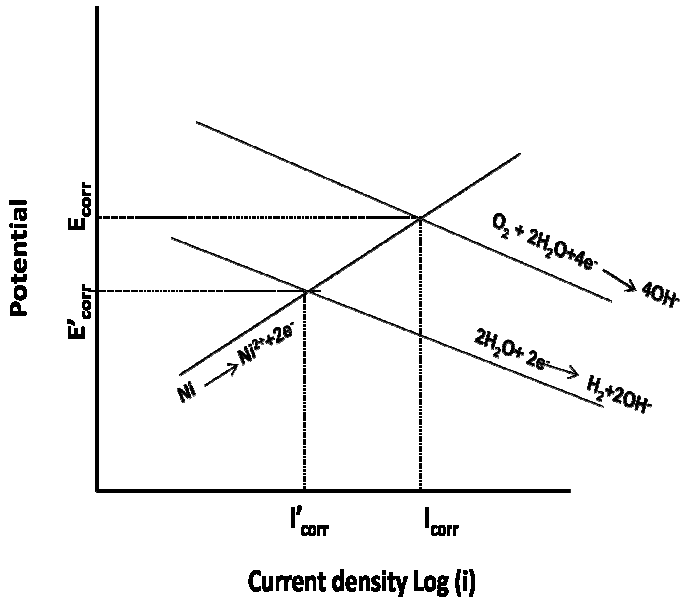

Figure 5.5 Evan's diagram presenting a schematic representation for the potentiodynamic behavior of bulk Ni in 3.5% NaCl aerated and deaerated solution. E_{corr} and E'_{corr} is the aerated and deaerated corrosion potential respectively, with I_{corr} and I'_{corr} being the corresponding corrosion current density.

Corrosion in NaCl solution is expected to cause pitting that typically initiates at grain boundaries and triple junctions. Such localized attack at these sites is expected to result in large deep pits. Figure 5.6 is a SEM micrograph showing the surface morphology of bulk Ni after potentiodynamic polarization testing in 3.5% NaCl solution up to a potential of 300 mV. The corroded surface displays dispersed pits of about 50 – 75 μm in diameter. Figure 5.7 presents the surface morphology of bulk Ni tested to a potential of 600 mV. It is clearly seen that for the same magnification, the corroded surface displays dispersed but larger deeper pits about 100 – 150 μm in diameter. In view of Figure 5.3, it is evident that within this potential range (300 to 600 mV) the

material is in the active region, so a higher potential simply leads to a higher corrosion rate as reflected in the pit morphology. Given the large grain size in the bulk Ni microstructure, these pits are rather widely spread. Figure 5.8 presents a higher magnification micrograph of the corrosion pit showing that the surface dissolution results in deep penetration along the grain boundaries revealing the grain structure.

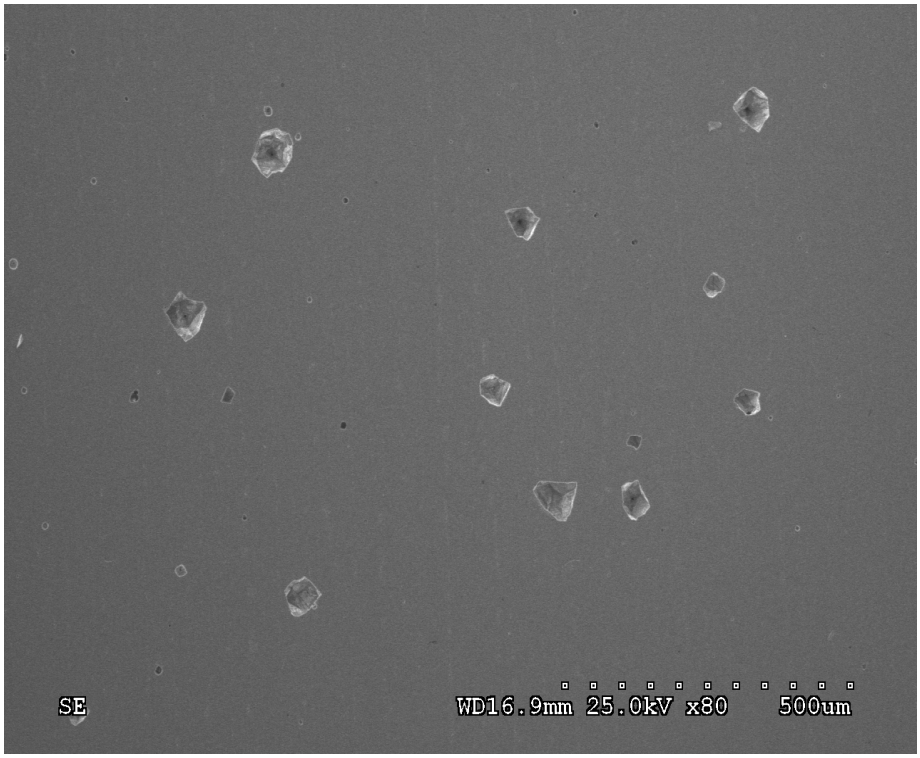

Figure 5.6 SEM micrograph showing the surface morphology of bulk Ni after potentiodynamic polarization testing in 3.5% NaCl aerated solution to an anodic potential of 300 mV.

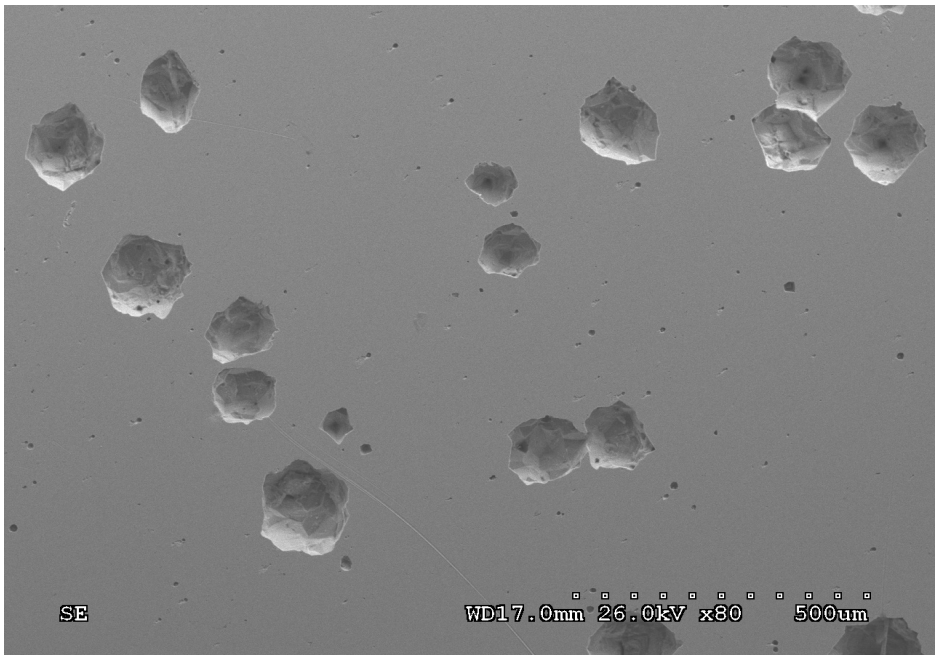

Figure 5.7 SEM micrograph showing the surface morphology of bulk Ni after potentiodynamic polarization testing in 3.5% NaCl aerated solution up to an anodic potential of 600 mV.

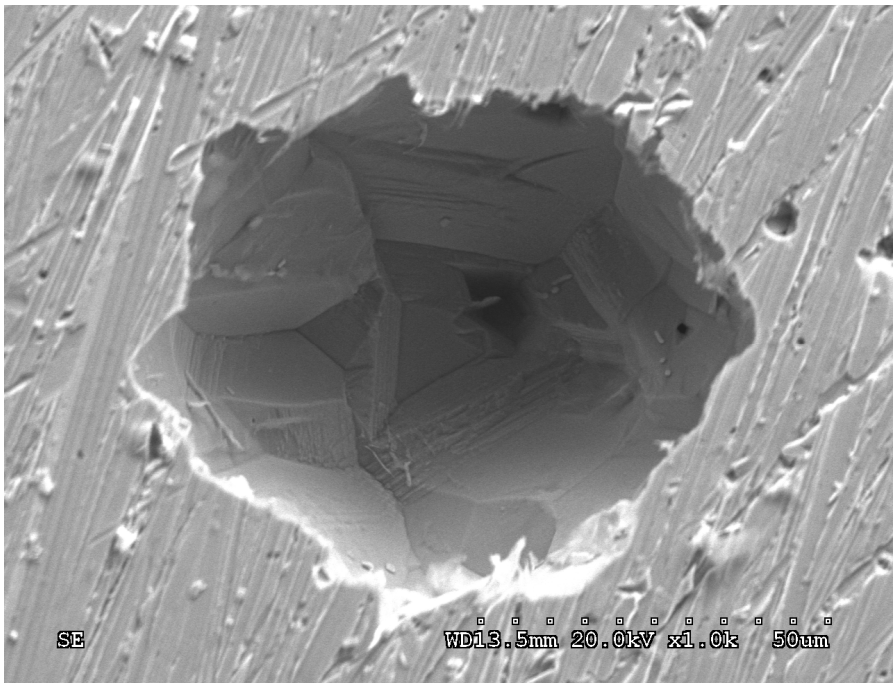

Figure 5.8 High magnification SEM micrograph showing the pitting morphology of bulk Ni after potentiodynamic polarization testing in 3.5% NaCl aerated solution to an anodic potential of 600 mV.

5.2.2 Corrosion Potential in 3.5% NaCl Solution

The equilibrium potential attained by the metal in the absence of electrical connections to the metal is called the corrosion potential or the OCP [5]. A stable OCP is taken to indicate that the system being studied has reached "steady state", i.e., the various corrosion reactions have assumed a constant equilibrium rate. The variation of OCP was studied in both aqueous environments.

Figure 5.9 shows the variation of OCP of bulk Ni in 3.5% NaCl aerated solution. It is evident that the OCP exhibits a slight increase and stabilizes at about -250 mV. Figure 5.15 is a micrograph showing the typical surface morphology after testing. A few small pits can be observed as the system is in equilibrium and there is no polarization.

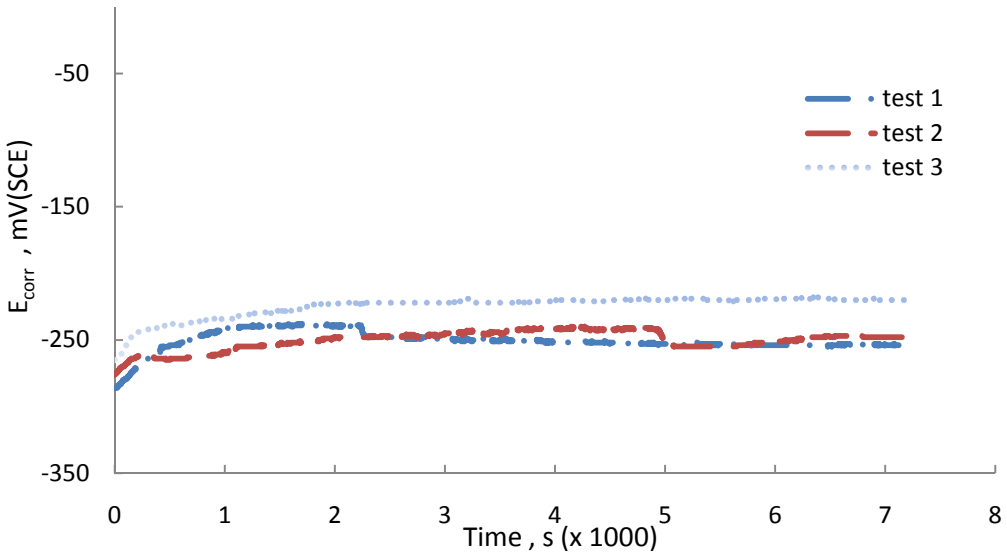

Figure 5.9 Open circuit potential variation as a function of time for bulk Ni in 3.5% NaCl aerated solution.

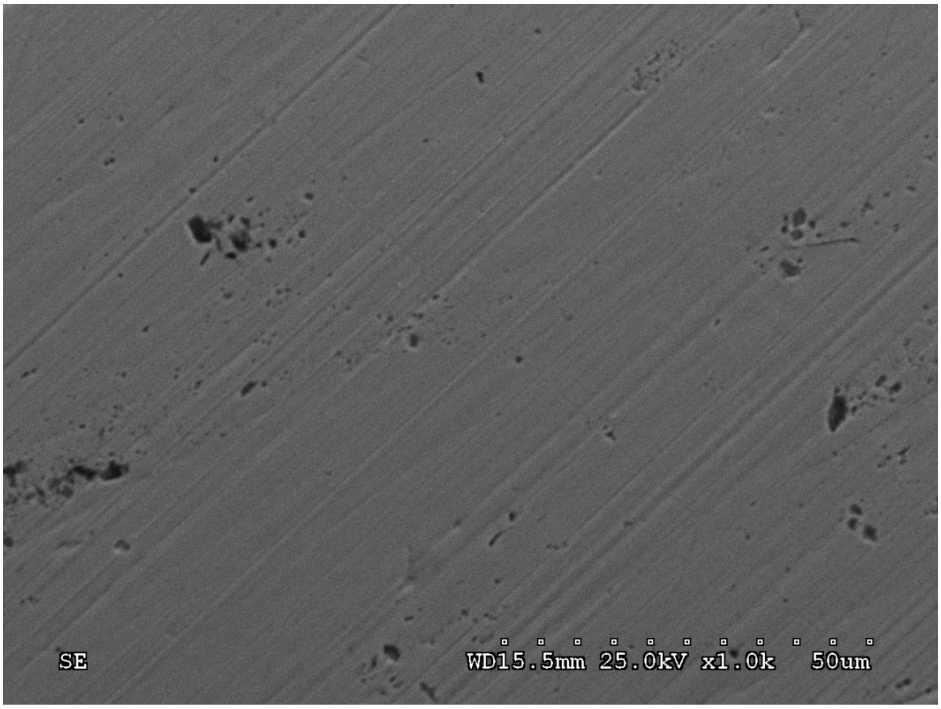

Figure 5.10 SEM micrograph showing surface morphology of bulk Ni after open circuit potential *vs* time testing in 3.5% NaCl aerated solution.

5.2.3 Surface Morphology Analysis

Surface morphology analysis was performed by profilometry to quantify the depth of the pits observed on the surface of bulk Ni after potentiodynamic polarization testing in 3.5% NaCl aerated solution to a potential of 600 mV. Figures 5.9 (a) and (b) present screen shots of the profile, (a) shows a pit depth of 35 μm and (b) pit depth of 59 μm. Similar analysis was conducted on various pits found on the surface and an average pit depth varying from 35 μm to 59 μm was obtained.

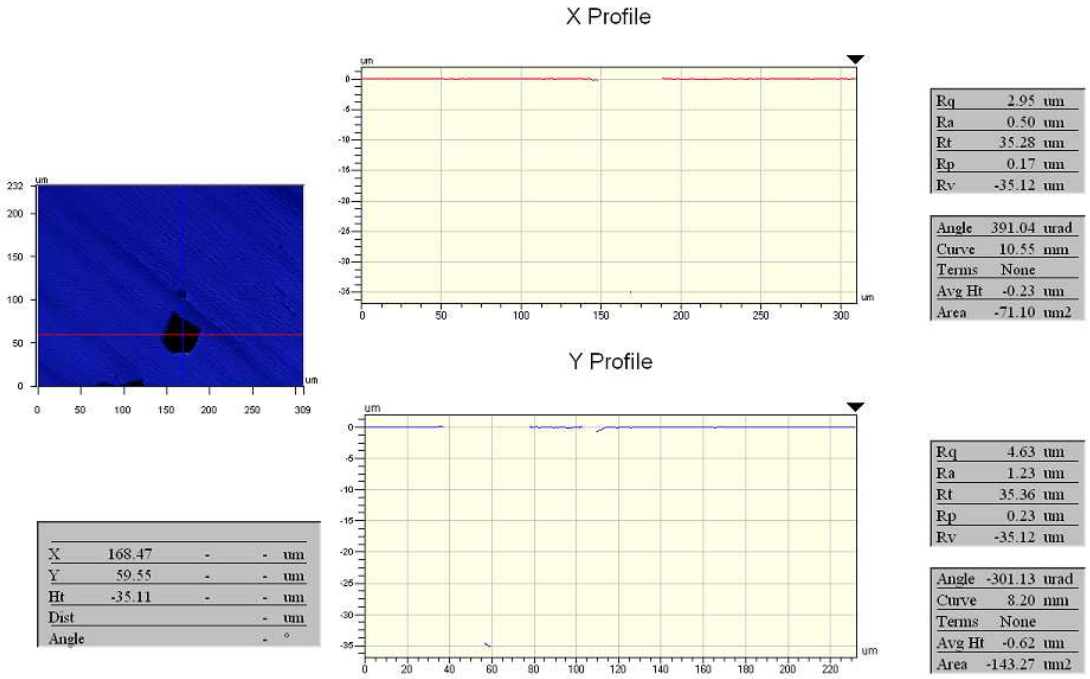

(a)

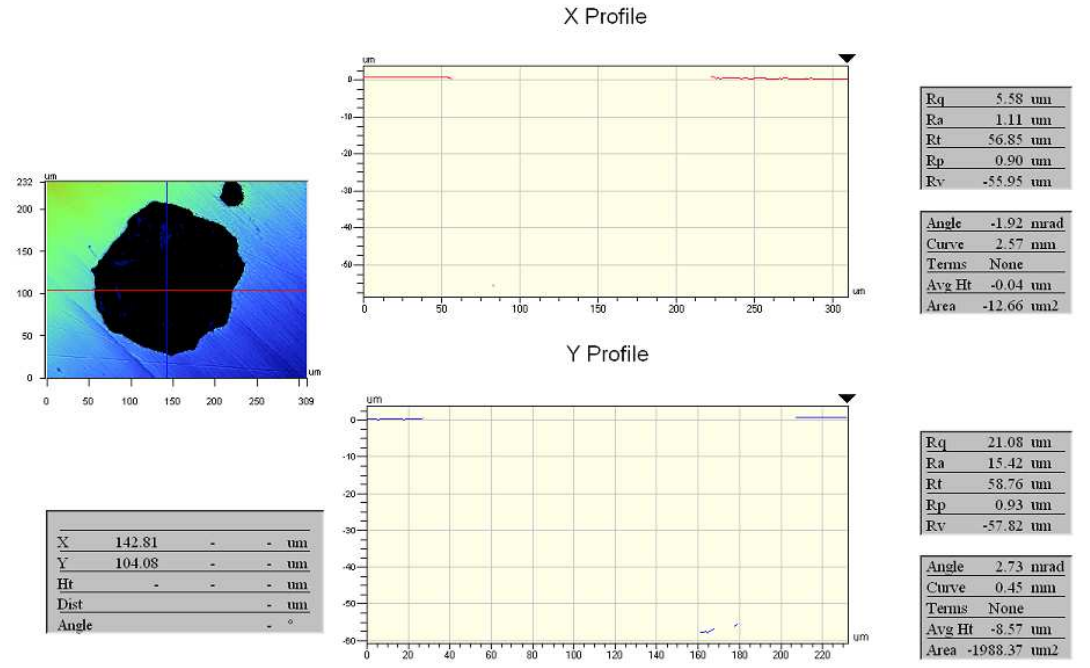

(b)

Figure 5.11 Screen shot (a) and (b) showing the depth profile of pits observed on the surface of bulk Ni after potentiodynamic polarization testing in 3.5% NaCl solution to a potential of 600 mV.

5.2.4 Potentiodynamic Polarization Response in 0.1N H_2SO_4 Solution

Potentiodynamic polarization tests were performed in 0.1N H_2SO_4 in both aerated and deaerated solutions. The electrochemical cell and electrode assembly was set up as described earlier in the experimental chapter.

Figure 5.12 presents the corrosion response of bulk nickel in 0.1N H_2SO_4 aerated solution. The metal exhibits active-passive behavior. Passivation [5] is defined as a condition of corrosion resistance due to formation of thin surface films under oxidizing conditions with high anodic polarization. It can be seen from Figure 5.12 that active dissolution occurs up to a potential of -200 mV, followed by a passive behavior. The activation polarization regime shows a high rate of increase that is significantly higher than that exhibited in the NaCl solution, Figure 5.3. At low potential, the corrosion rate measured by anodic current density is high and increases further with potential in the active region. Above the primary passivation potential E_{pp} (approximately -200 mV in this case) a passive film starts developing inhibiting further increase in current density with the increase in potential. In this regime, a passive film starts forming at the surface. It is interesting to note that just above 0 mV, a more dramatic decrease in the current density is observed with an i_p value of around 0.2 μAcm^{-2} denoting the formation of a stable oxide surface film. Based on thermodynamics, the first passivation stage (-200 to 0 mV) is associated with the formation of Ni $(OH)_2$ while the second passivation regime is associated with the presence of stable Ni_3O_4 and Ni_2O_3.

It can be seen from Table 5.4 that the average corrosion potential in aerated 0.1N H_2SO_4 solution was found to be -273 mV and the average corrosion current density was 38 μAcm^{-2}. Again, this current density is higher than that observed in NaCl since in this case a second cathodic reaction operates. This reaction is hydrogen reduction, causing an increase in the cathodic current density and thus, the corrosion rate

$$H^+ + 2e^- \longrightarrow H_2 \qquad (7)$$

Enhanced hydrogen reduction kinetics occur at the grain boundaries,

$$Ni + 2H_2O \longrightarrow Ni(OH)_2 + 2H^+ + 2e^- \quad (8)$$

$$3Ni + 4H_2O \longrightarrow Ni_3O_4 + 8H^+ + 6e^- \quad (9)$$

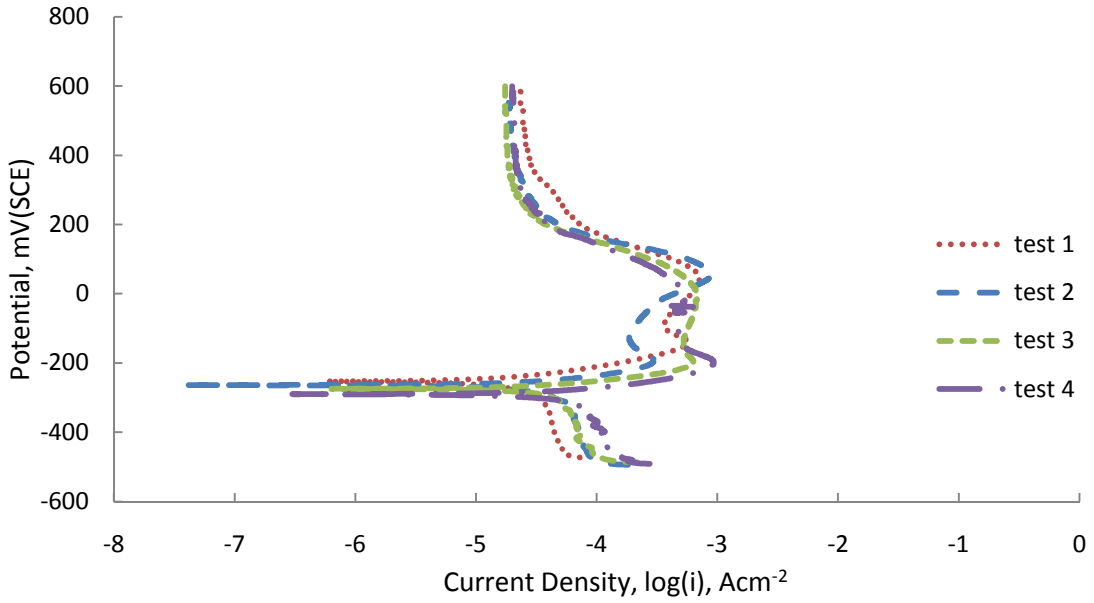

Figure 5.12 Potentiodynamic polarization behavior of bulk Ni in 0.1N H_2SO_4 aerated solution.

Table 5.4 Potentiodynamic Polarization Test Results of Bulk Ni in 0.1N H_2SO_4 Aerated Solution.

Parameter	test 1	test 2	test 3	test 4	Average Value ±SD
Corrosion Potential (mV)	-255.6	-266.9	-277.2	-292.6	-273.0 ±13.6
Corrosion Rate ($\mu A.cm^{-2}$)	35.5	40.8	31.2	44.0	38.0 ±4.8

SD: Standard Deviation

Figure 5.13 presents the corrosion response of bulk nickel in 0.1N H_2SO_4 deaerated solution. Active-passive behavior is exhibited similar to that in the aerated environment. Active dissolution occurs to a potential of around -200 mV. Then, passivity starts and a second passive state is exhibited at a potential of about 200 mV, which is similar to the behavior in aerated environment.

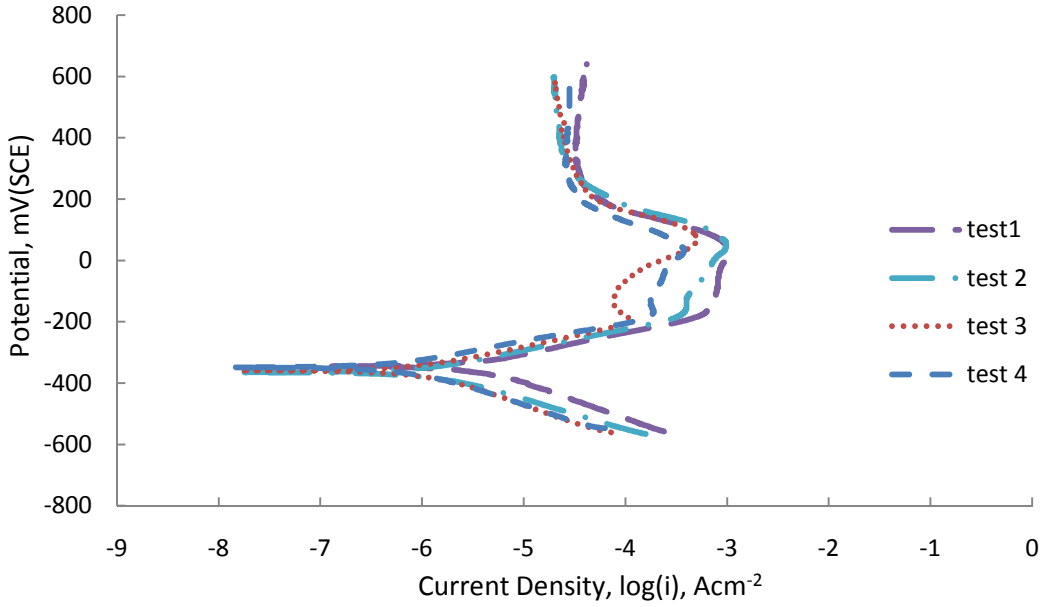

Figure 5.13 Potentiodynamic polarization behavior of bulk Ni in 0.1N H_2SO_4 deaerated solution.

Table 5.5 Potentiodynamic Polarization Test Results of Bulk Ni in 0.1N H_2SO_4 Deaerated Solution.

Parameter	test 1	test 2	test 3	test 4	Average Value ±SD
Corrosion Potential (mV)	-346.3	-365	-359.7	-348.5	-354.8 ±7.6
Corrosion Rate ($\mu A.cm^{-2}$)	3.66	1.26	1.20	1.14	1.82 ±1.1

SD: standard deviation

The polarization behavior of bulk Ni in the two environments can be compared by constructing an Evan's diagram (potential vs. current density). Figure 5.14 graphically represents the behavior of bulk Ni in aerated and deaerated 0.1N H_2SO_4 solution .The anodic and cathodic reactions mentioned earlier are shown schematically on the graph. E_{corr} is the aerated corrosion potential E'_{corr} is the deaerated corrosion potential, with I_{corr} and I'_{corr} being the corresponding corrosion current density.

From Table 5.4 it can be seen that the average corrosion potential was found to be -354 mV, which is almost 100 mV lower compared to the aerated environment and the average current density for the deaerated environment was found to be 1.81 $\mu Acm^{-2.}$ The average corrosion current in the aerated 0.1N H_2SO_4 solution is almost forty times higher due to the incorporation of O_2 in the cathodic reaction, $O_2 + 4H^+ + 4e^- \longrightarrow 4OH^-$ causing an increase in the cathodic current density and thus, the corrosion rate.

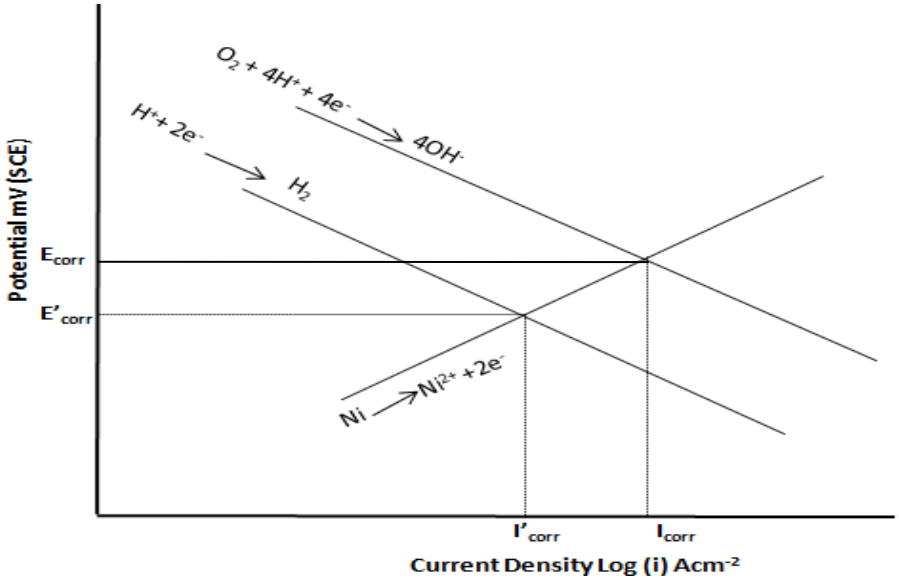

Figure 5.14 Schematic representation of Evan's diagram for the potentiodynamic behavior of bulk Ni in 0.1N H_2SO_4 aerated and deaerated solution. E_{corr} and E'_{corr} are the aerated and deaerated corrosion potential respectively with I_{corr} and I'_{corr} being the corresponding corrosion current density.

Figure 5.15 shows the surface morphology of the corroded surface in 0.1N H_2SO_4 aerated solution. Dispersed small pits are present when compared to the pits formed in 3.5% NaCl solution under the same operating conditions. This is due to the active-passive behavior of bulk Ni in 0.1N H_2SO_4 solution.

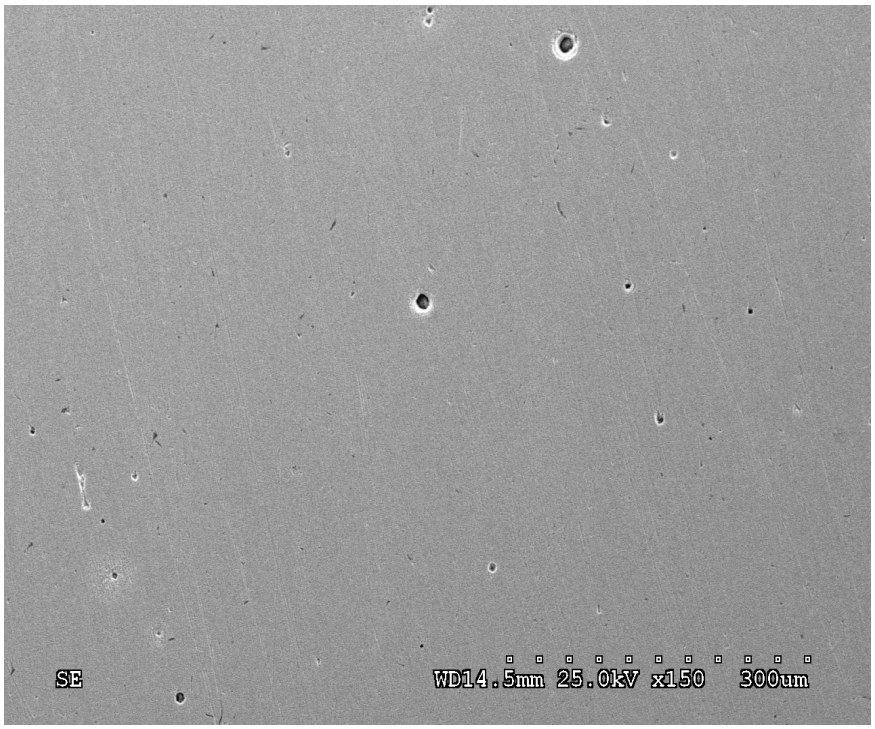

Figure 5.15 SEM micrograph showing the surface morphology of bulk Ni after potentiodynamic polarization testing in 0.1N H_2SO_4 aerated solution.

5.2.5 Corrosion Potential in 0.1N H_2SO_4 Solution

Figure 5.16 presents the OCP variation of bulk Ni in 0.1N H_2SO_4 in aerated solution. The system attains stability at a potential of around -260 mV, which is more anodic than the values obtained in the potentiodynamic polarization results, where the average value is around -354 mV. Figure 5.17 is a micrograph showing typical surface morphology after testing. A few small pits can be observed as the system attains equilibrium.

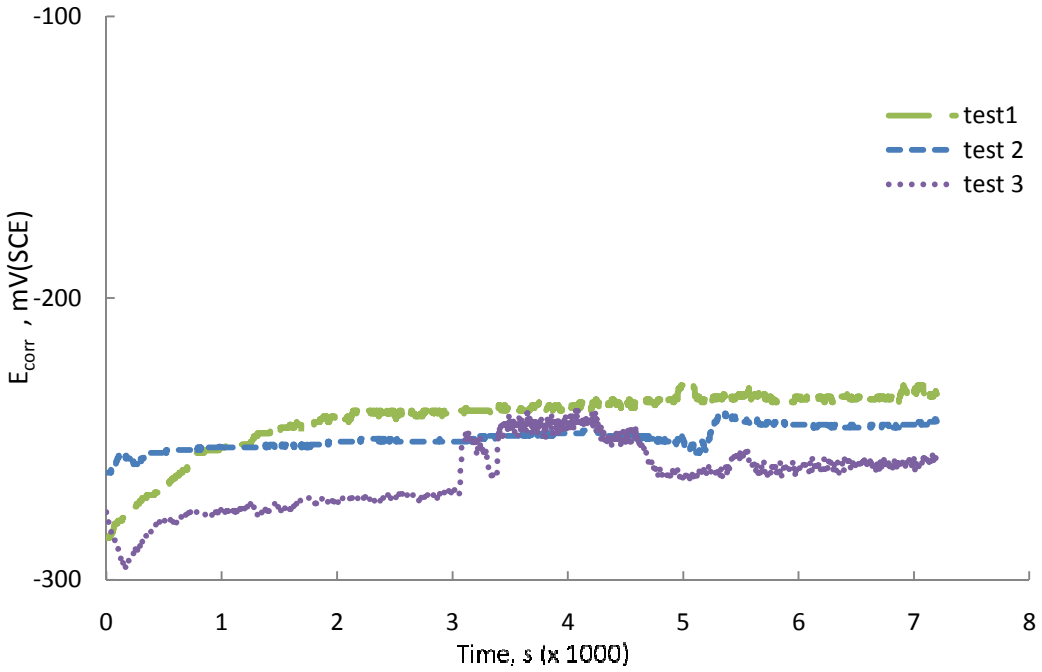

Figure 5.16 Open circuit potential variation as a function of time for bulk Ni in 0.1N H_2SO_4 aerated solution.

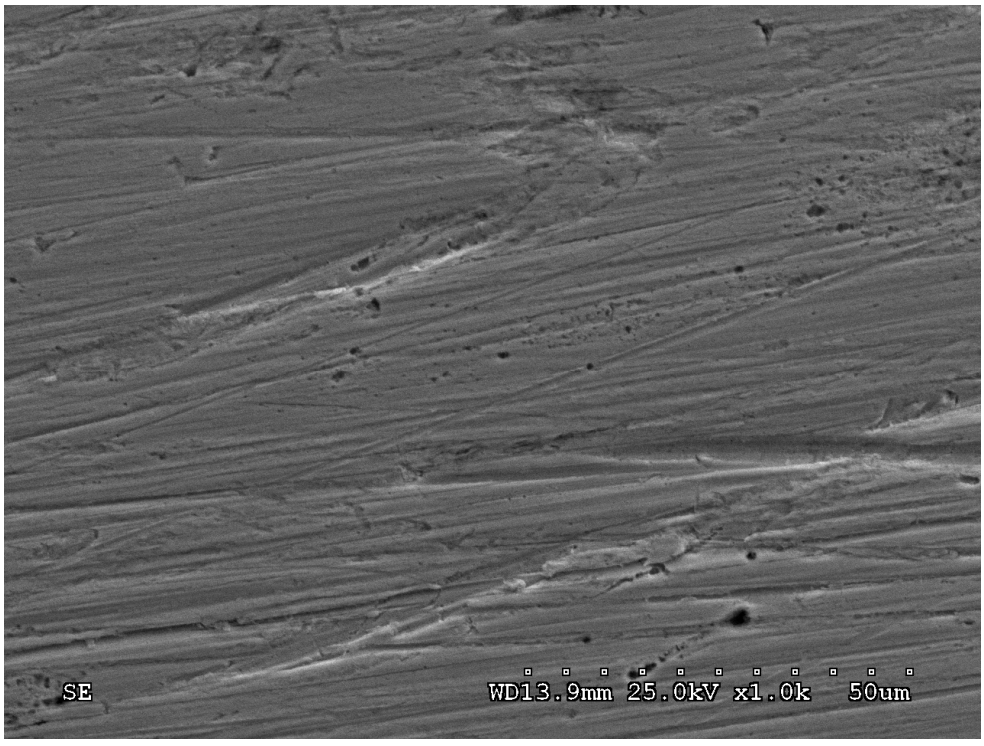

Figure 5.17 SEM micrograph showing surface morphology of bulk Ni after open circuit potential *vs* time testing in 0.1N H_2SO_4 aerated solution.

5.3 Corrosion Behavior of Nanocrystalline Nickel

5.3.1 Potentiodynamic Polarization Response in 3.5% NaCl Solution

Figure 5.18 presents the potentiodynamic polarization response of nano Ni in aerated 3.5% NaCl solution. The anodic polarization curves exhibit high consistency. Nanocrystalline Ni exhibits activation polarization. The observed behavior is in agreement with previous corrosion study in NaCl solution [21] exhibiting active dissolution behavior. Table 5.6 presents the average corrosion potential and corrosion rate of nano Ni in 3.5% NaCl aerated solution.

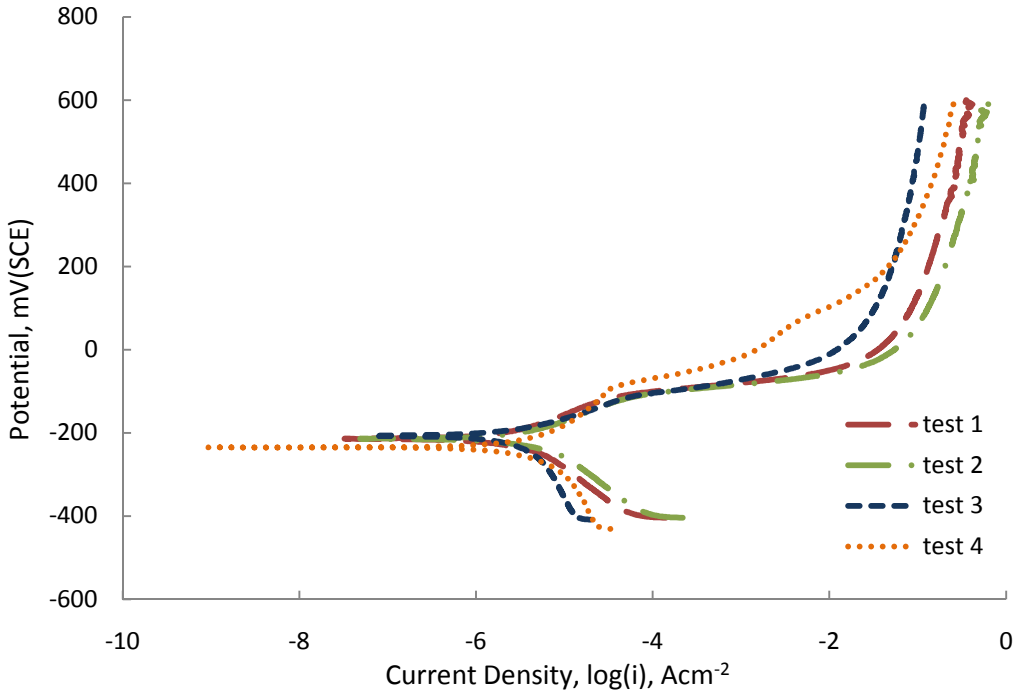

Figure 5.18 Potentiodynamic polarization behavior of nano Ni in 3.5% NaCl aerated solution.

Table 5.6 Potentiodynamic Polarization Test Results of Nano Ni in 3.5% NaCl Aerated Solution.

Parameter	test 1	test 2	test 3	test 4	Average Value ±SD
Corrosion Potential (mV)	-251.1	-214.1	-209.1	-235.3	-227.4 ±16.9
Corrosion Rate ($\mu A.cm^{-2}$)	3.67	3.95	3.83	3.92	3.84 ±0.1

SD: Standard Deviation

The potentiodynamic polarization behavior of nano Ni in 3.5% NaCl deaerated solution is presented in Figure 5.19. The general response is similar to that in the aerated environment. Table 5.7 shows the value of average corrosion potential to be -285 mV, which is around 60 mV lower than the potential observed in the aerated environment. Although the difference in potential is considerably low in aerated and deaerated solutions, the average corrosion rate in deaerated solution is 0.03 μAcm^{-2} which is two orders of magnitude lower compared with that of 3.8 μAcm^{-2} as seen in the aerated solution. Even though a lower corrosion rate is expected for the deaerated environment, the reason for such a dramatic reduction is not clear at present.

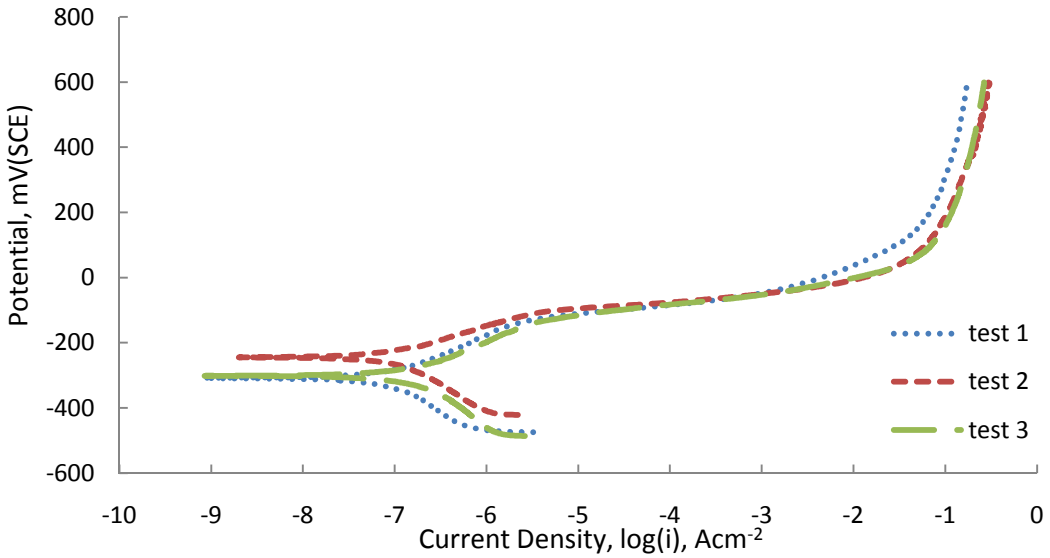

Figure 5.19 Potentiodynamic polarization behavior of nano Ni in 3.5% NaCl deaerated solution

Table 5.7 Potentiodynamic Polarization Test Results of Nano Ni in 3.5% NaCl Deaerated Solution.

Parameter	test 1	test 2	test 3	Average Value ±SD
Corrosion Potential (mV)	-309.3	-244.7	-301.1	-285.0 ±28.7
Corrosion Rate ($\mu A.cm^{-2}$)	0.014	0.072	0.013	0.03 ±0.02

It is known from the literature that nanomaterials have higher volume fraction of atoms associated with the intercrystalline defects such as grain boundaries and tripe junctions in the material. Wang [21] studied the grain size dependence of intercrystalline volume fraction analysis to calculate intercrystalline surface fraction and the crystal/intercrystalline surface ratio, to correlate these factors with the corrosion behavior of nanocrystalline materials. It was suggested that the enhanced intercrystalline surface fraction may increase the overall dissolution rate and result in a poor corrosion performance of nanocrystalline materials (as described earlier in chapter 3).

Szklarska et al. [26] found that nanocrystalline pure materials showed lower passivation current densities and higher pitting potential in solutions containing Cl^- ions. It is argued that due to grain size reduction to the nano meter scale, the passive oxide film formation and pitting reduces due to the uniform distribution of defects in the passive film. It was also suggested that the accumulation of Cl^- ions in such shallow defects is more difficult and a higher driving force is required to penetrate the oxide film in comparison to materials with deeper defects as expected in their bulk counterparts.

Figure 5.20 (a) presents the surface morphology of nano Ni tested in aerated 3.5% NaCl solution up to an anodic potential of 300 mV and (b) is a high magnification of one of the pits. It is interesting to note a bimodal pit distribution. A high population of uniformly distributed fine pits

approximately 1-2 μm in diameter is clearly discerned in Figure 5.20 (a) along with dispersed larger pits 20 – 100 μm diameter.

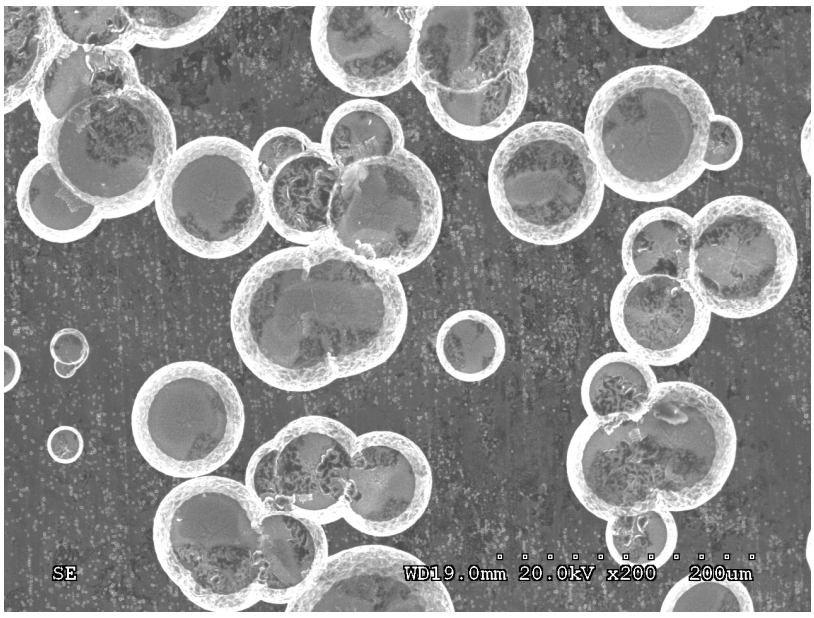

(a)

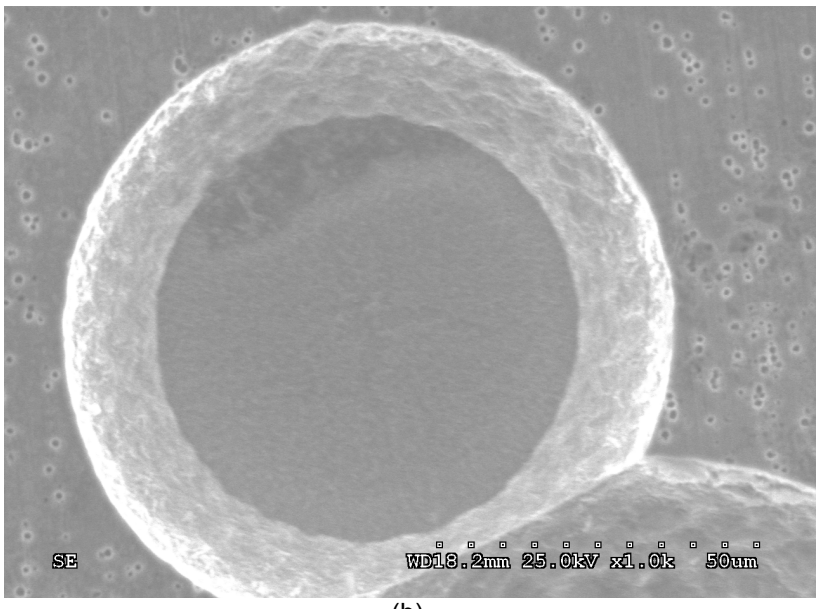

(b)

Figure 5.20 (a) SEM micrograph showing the surface morphology of nano Ni tested in 3.5% NaCl aerated solution up to an anodic potential of 300 mV (b) High magnification SEM micrograph of one of the pits

The higher density of submicron pits compared to those in bulk metals is in agreement with previous studies and the uniformity arises from the increased volume fraction of grain boundaries in the nanocrystalline material. With a decrease in grain size, the number of triple junctions increases which results in the increase in number of pits but a decrease in size of the pits. The pits in the nanocrystalline material become small and finely distributed. This evidence shows that uniform high density pitting initiates at grain boundaries but growth occurs in a very small fraction of these pits.

During pitting Cl^- concentration builds up and when a critical concentration is reached "breakaway" growth occurs. Preferential pit growth will occur in those pits that reached critical conditions first while pitting will cease on the rest of the pits. At this point, all the cathodic current requirement will come from the dissolution process in the dispersed larger pits causing their continuous growth. It should be noted however that the density of the larger pits is still higher than that observed in bulk metals. This observation helps to clarify the pitting mechanism in nanocrystalline metals, i.e., the initial anodic current density comes from numerous uniformly distributed submicron nano pits. The moment that critical conditions develop, a much smaller number of pits break away and grow. The anodic current is now supported by these growing pits.

Figure 5.21 presents the surface morphology of nano Ni in 3.5% NaCl aerated solution tested to an anodic potential of 600 mV. It is evident that with an increase from 300 mV to 600 mV there is an increase in the diameter of the pits due to the increased anodic current density. As known from corrosion theory, current density rather than current is proportional to corrosion rate. Since the same current is concentrated into a smaller surface area, it results in an increased local corrosion rate. Corrosion rate is inversely proportional to area for the same dissolving current thus, localized pit growth takes place.

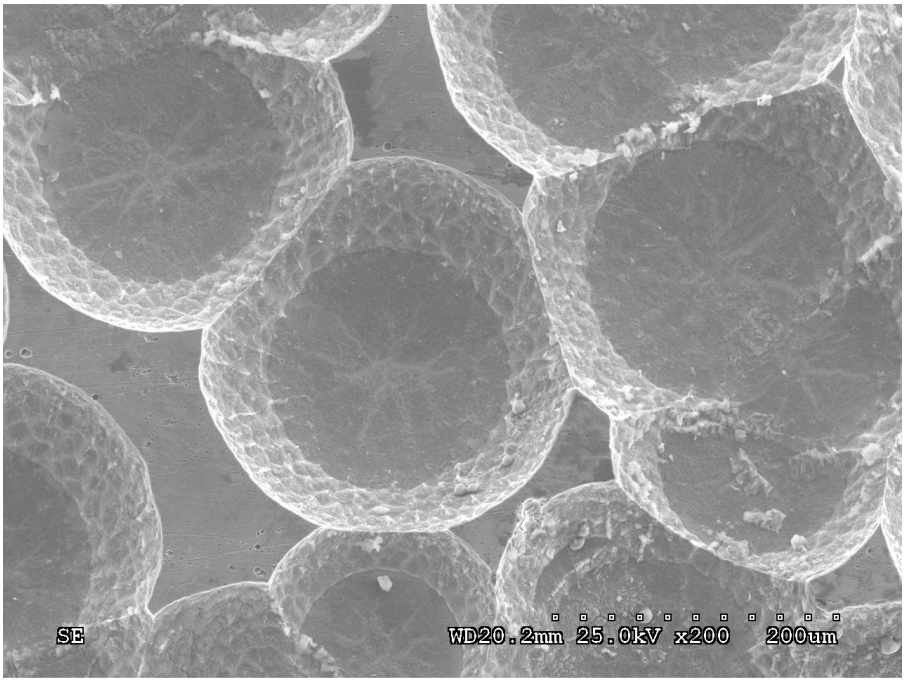

Figure 5.21 SEM micrograph showing the surface morphology of nano Ni after potentiodynamic polarization testing in 3.5% NaCl aerated solution to a potential of 600 mV.

Figure 5.22 presents a scanning electron micrograph showing the typical surface morphology and a high magnification SEM image from the interior of a pit developed in 3.5% NaCl. It can be clearly seen from the images that the attack is shallow and does not penetrate deep as seen in bulk Ni shown in Figure 5.8. Furthermore, the high magnification image clearly shows fine dissolution characteristics on the pit surface. Dissolution at the grain boundary of the nano Ni is expected to generate the observed morphology. The evidence also shows another distinct difference in pit growth and formation between nano and bulk Ni. Pits in nano Ni grow in two directions. The higher growth occurs downwards since, as known gravity drives pitting. Pits grow laterally, at a slower pace. The lateral growth creates the “rim” observed in all pits in nano Ni. This is resulting from the high density of grain boundaries present in nano Ni that still provide sensitive corrosion sites. On the contrary, such high density of grain boundaries is not present in the bulk and pitting follows the high angle large boundaries. Figure 5.23 (a) provides a schematic presenting the pitting process in nano Ni. Figure 5.23 (b) presents a high magnification SEM image showing details of the lateral growth. A comparison of rim and pit sizes in Figure 5.20

further verifies that pit grows both vertically and laterally (i.e., smaller pits are associated with narrow rims).

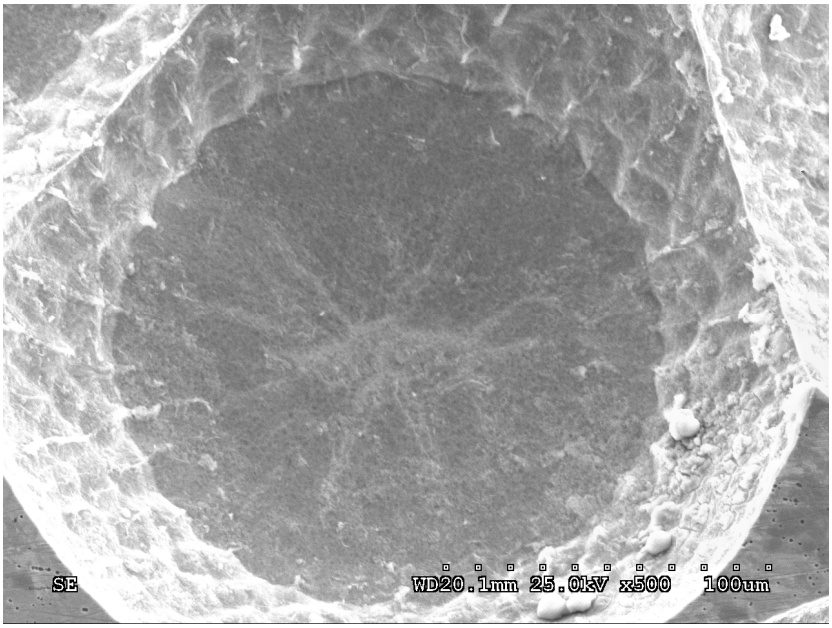

(a)

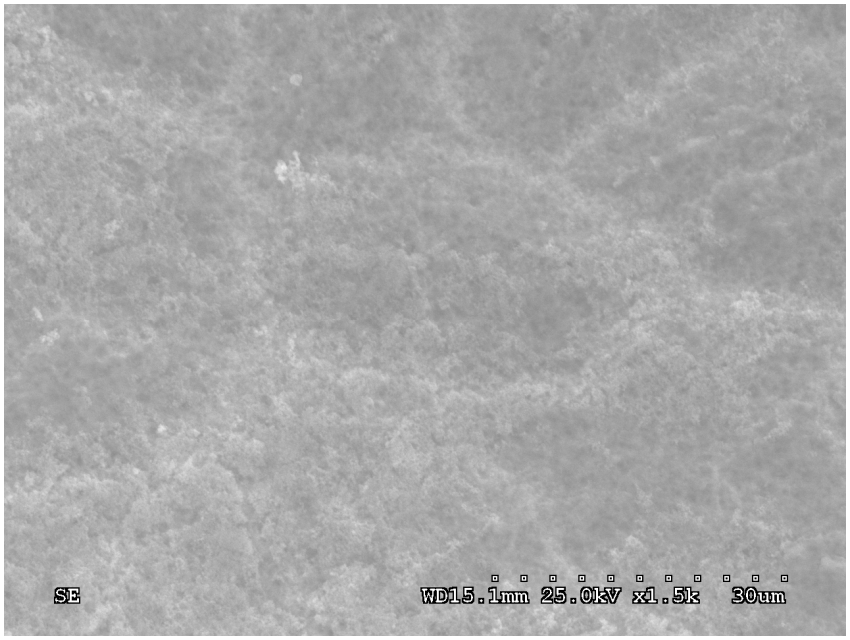

(b)

Figure 5.22 SEM micrograph of (a) a pit observed on the surface of nano Ni after potentiodynamic testing in 3.5% NaCl aerated solution and (b) high magnification image of the pit interior.

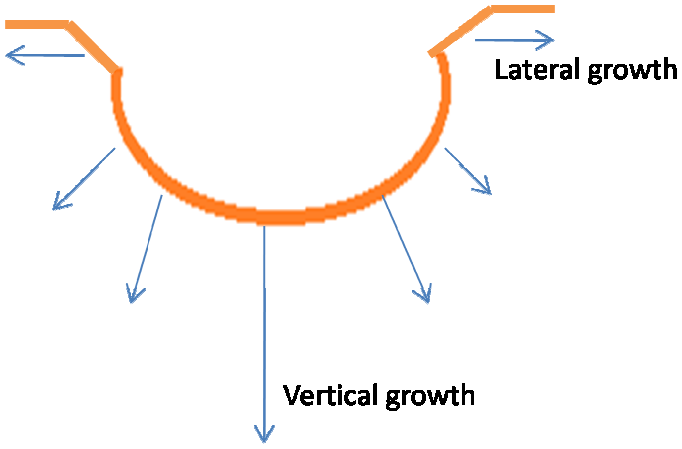

(a)

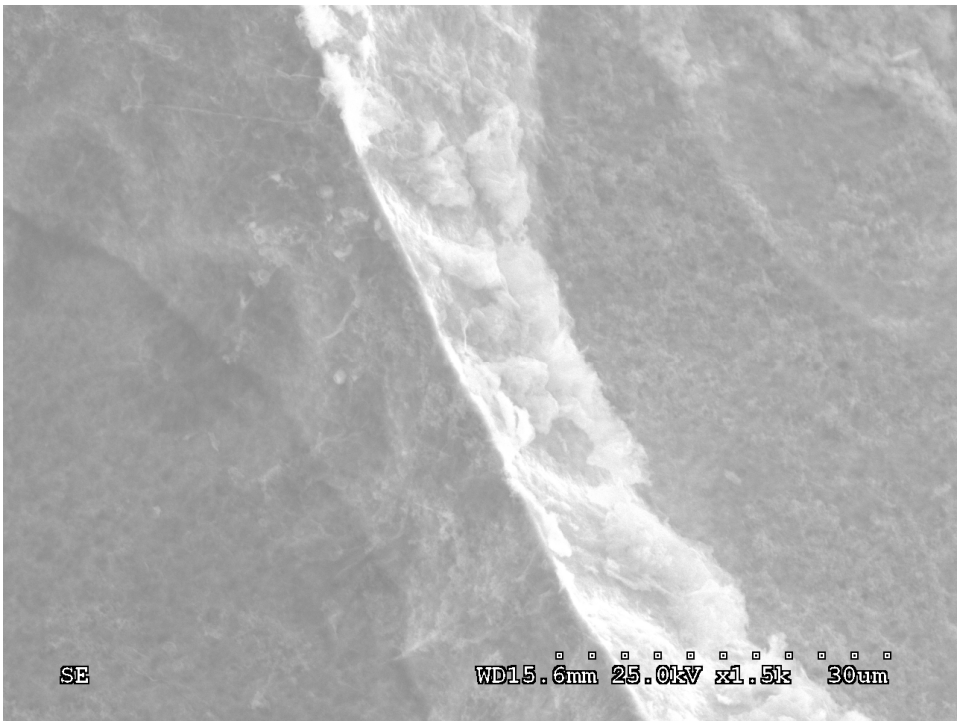

(b)

Figure 5.23 (a) Schematic presenting the pitting process in nano Ni and (b) High magnification SEM micrograph showing details of lateral pit growth in nano Ni.

5.3.2 Corrosion Potential in 3.5% NaCl Solution

Corrosion potential variation as a function of time was observed in 3.5% NaCl aerated solution. Figure 5.24 presents the open circuit potential response of nano Ni in 3.5% NaCl aerated solution. The value of corrosion potential from potentiodynamic polarization in Table 5.6 is slightly more anodic compared to the values observed. The corrosion potential has a low value initially but with time rises and stabilizes just above -200 mV. Figure 5.25 shows the surface morphology of nano Ni after testing. Very few, if any, pits can be observed in contrast to the bulk Ni where few small pits are clearly visible in Figure 5.10. Figure 5.24 and the SEM surface observations Figure 5.25 show that the nano Ni has a stable behavior.

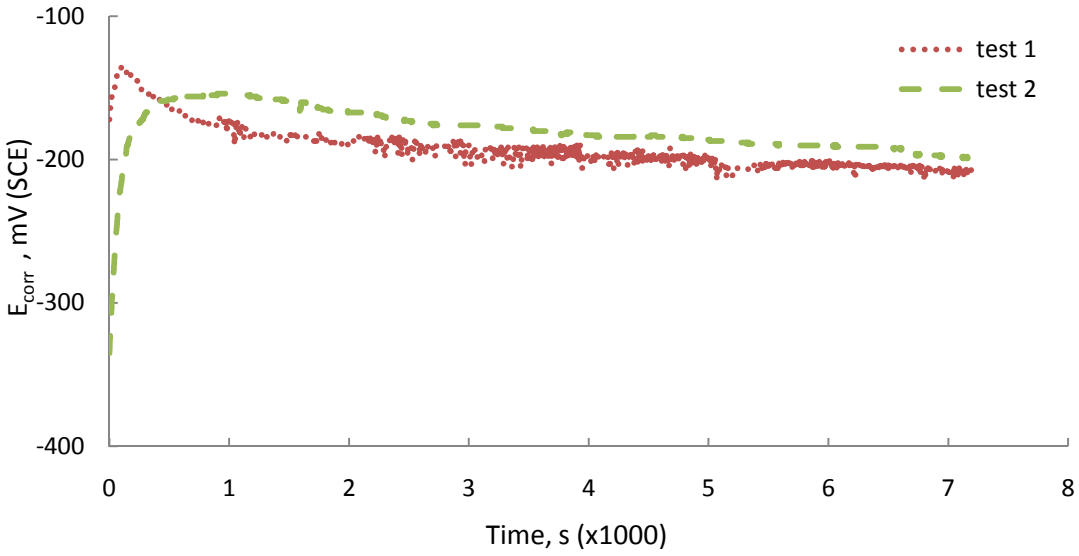

Figure 5.24 Open circuit potential as a function of time for nanocrystalline Ni in 3.5% aerated NaCl solution.

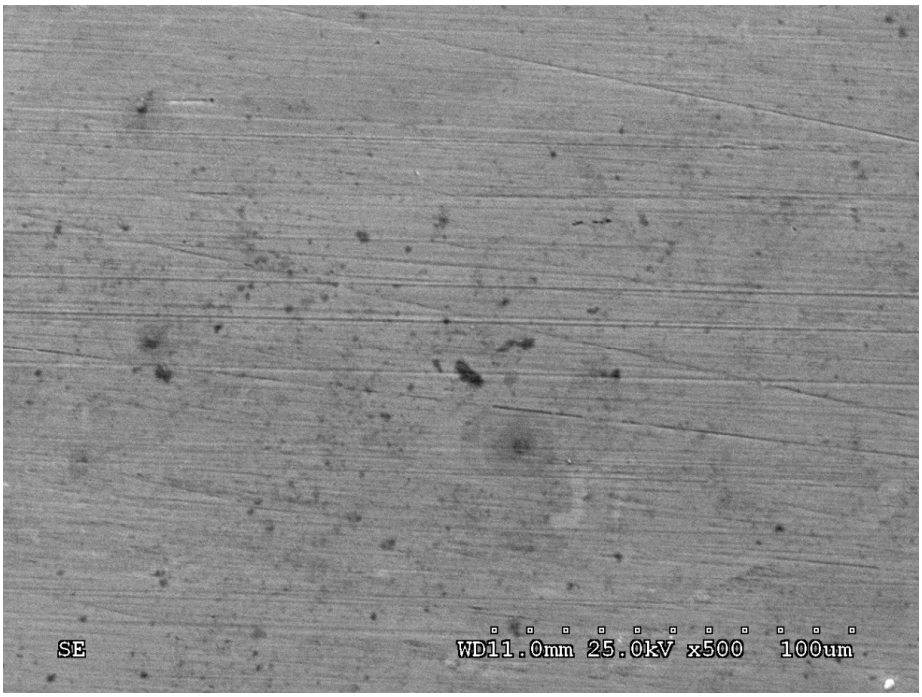

Figure 5.25 SEM micrograph showing surface morphology of nano Ni after open circuit potential vs. time testing in 3.5% NaCl aerated solution.

5.3.3 Surface Morphology Analysis

Surface morphology analysis was performed by profilometry to quantify the size of the pits observed on the surface of nano Ni after potentiodynamic polarization testing in aerated 3.5% NaCl solution up to a potential of 600 mV. Figure 5.26 (a) and (b) present screen shots of the profile, showing pit depths of 44 μm and 45 μm. Similar analysis was conducted on several pits found on the surface and revealed an average pit depth from 40 μm to 45 μm. This is contrary to the depth observed in the bulk Ni where the average pit depth varied from 35 μm to 59 μm, indicating that pitting is more uniform on the nano Ni.

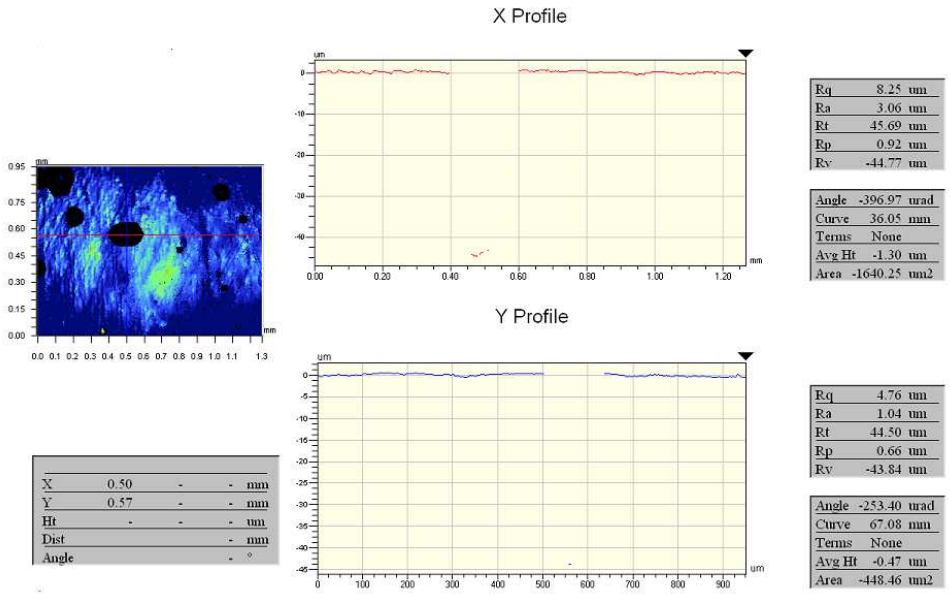

(a)

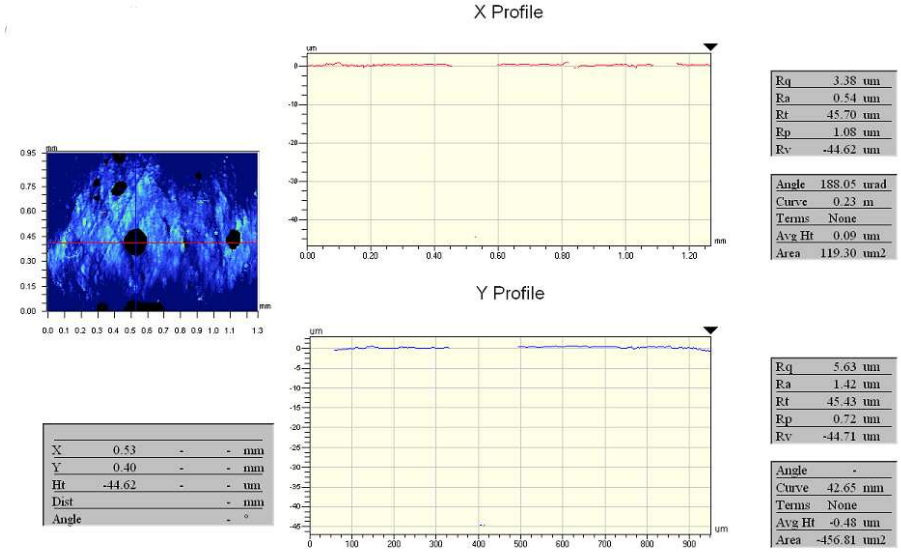

(b)

Figure 5.26 (a) and (b) Screen shots showing the depth profile of pits observed on the surface after potentiodynamic polarization testing of nano Ni in 3.5% NaCl solution to a potential of 600 mV.

5.3.4 Potentiodynamic Polarization Response in 0.1N H_2SO_4 Solution

Figure 5.27 presents the potentiodynamic polarization response of nano Ni in 0.1N H_2SO_4 aerated solution. An activation behavior is observed extending from about -200 mV to 100 mV. Although passivation was observed in previous corrosion studies in 2N H_2SO_4 [28], the present studies show that passivation does not take place in 0.1N H_2SO_4 solution. Table 5.8 presents the values of the corrosion potential and corrosion rate of all tests conducted in 0.1N H_2SO_4 aerated solution. It can be seen from Table 5.8 that the average corrosion potential was found to be -212 mV and the average corrosion current density was around 211 μAcm^{-2}.

Figure 5.28 presents the corrosion response of nano Ni in 0.1N H_2SO_4 deaerated solution. An activation behavior is observed which is similar to that observed in the aerated environment. Differences are evident in the corrosion potential and corrosion current density values. This is due to the absence of oxygen resulting in the reduction of cathodic reaction.

Table 5.9 presents the average corrosion potential in deaerated environment was found to be -353 mV and average corrosion current density was 2.0 $\mu A.cm^{-2}$. As expected, the corrosion potential and corrosion current density values in the deaerated solution were much lower compared to the values observed in the aerated environment. It is interesting to note that similar to the behavior in NaCl solution, the corrosion rate in the deaerated 0.1N H_2SO_4 solution is also two orders of magnitude lower to that in the aerated solution. This seems to suggest that in the absence of oxygen, reduction reaction kinetics can be significantly reduced on the surface of nanocrystalline Nickel.

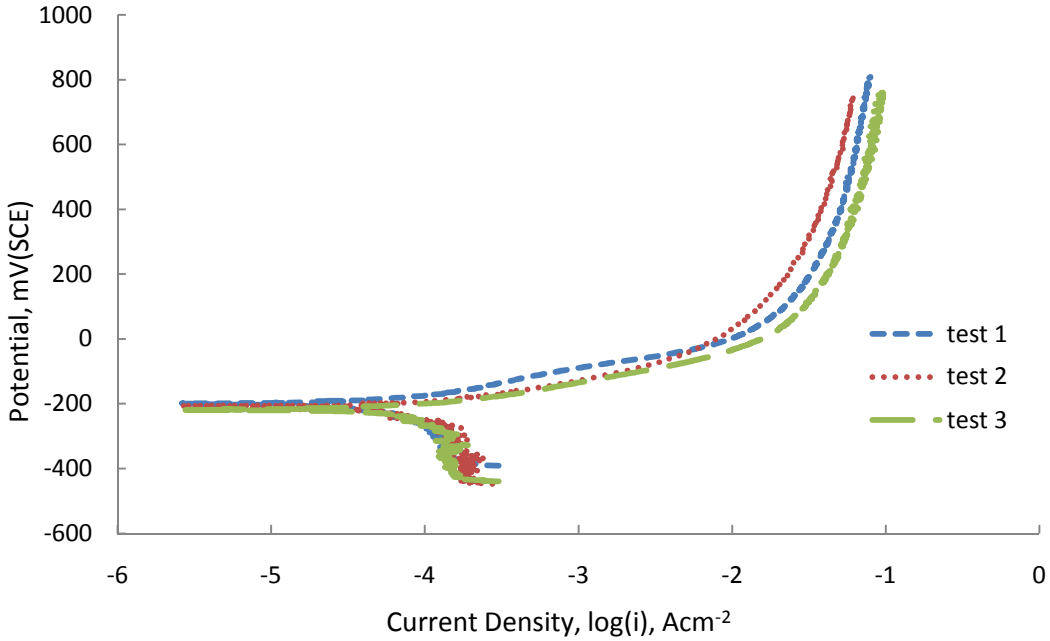

Figure 5.27 Potentiodynamic polarization behavior of nano Ni in 0.1N H_2SO_4 aerated solution.

Table 5.8 Potentiodynamic Polarization Test Results of Nano Ni in 0.1N H_2SO_4 Aerated Solution.

Parameter	test 1	test 2	test 3	Average Value ±SD
Corrosion Potential (mV)	-218.5	-213.8	-202.5	-211.6 ±6.7
Corrosion Rate ($\mu A.cm^{-2}$)	203.66	217.16	212.16	211.0 ±5.5

SD: standard deviation

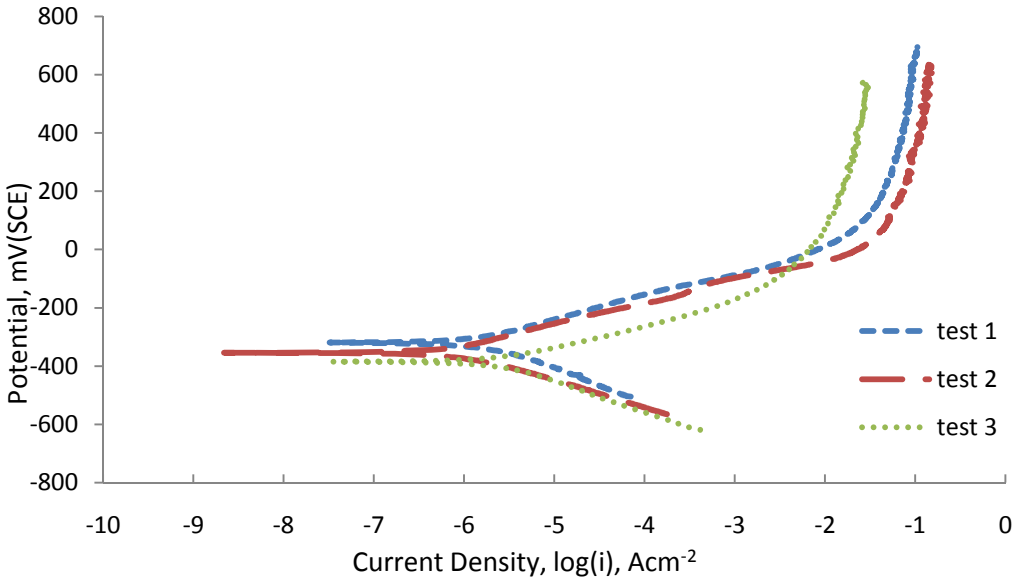

Figure 5.28 Potentiodynamic polarization behavior of nano Ni in 0.1N H_2SO_4 deaerated solution.

Table 5.9 Potentiodynamic Polarization Test Results of Nano Ni in 0.1N H_2SO_4 Deaerated Solution.

Parameter	test 1	test 2	test 3	Average Value ±SD
Corrosion Potential (mV)	-319.5	-385.5	-353.5	-353 ±26.9
Corrosion Rate ($\mu A.cm^{-2}$)	2.04	2.13	2.12	2.10 ±0.03

Figure 5.29 presents the surface morphology of nano Ni after potentiodynamic polarization testing in 0.1N H_2SO_4 aerated solution. The micrograph reveals a corrosion process producing some characteristic features. In view of Figure 5.27 and the corrosion rate reported in Table 5.8, it is clear that the particular morphology develops after significant dissolution at the surface. Furthermore, it can be seen in Figure 5.30 (a) that the corrosion attack at the surface of the material is rather uniform and does not penetrate locally as seen in the bulk Ni, Figure 5.11, for similar operating conditions. It is interesting that this uniform surface attack causes a "polishing" effect, revealing structural details along with a periodicity in its occurrence developing

a particular pattern. The higher sensitivity of the grain boundaries is evident in the high magnification micrograph in Figure 5.30 (b). It is interesting to note that some patterning results from the latter sensitivity producing rather uniform features 40 μm in size. Formation of these features may also be associated with impurity segregation and conditions during electrodeposition.

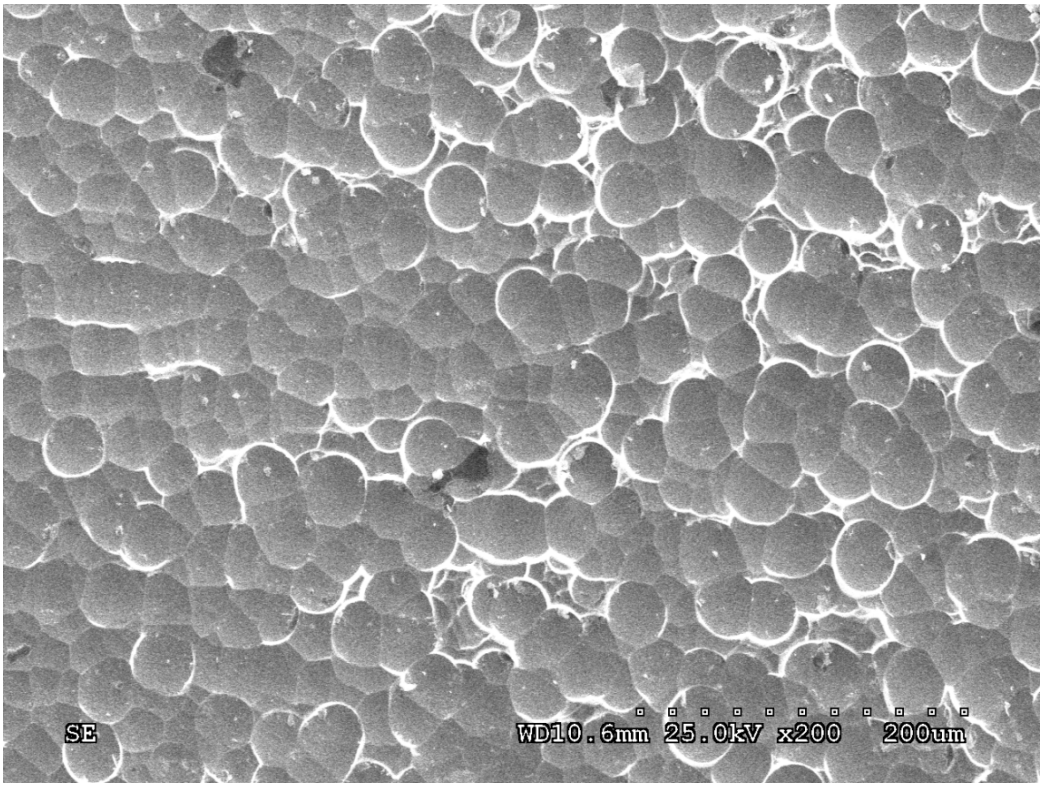

Figure 5.29 SEM micrograph showing the surface morphology of nano Ni after potentiodynamic polarization testing in 0.1N H_2SO_4 aerated solution.

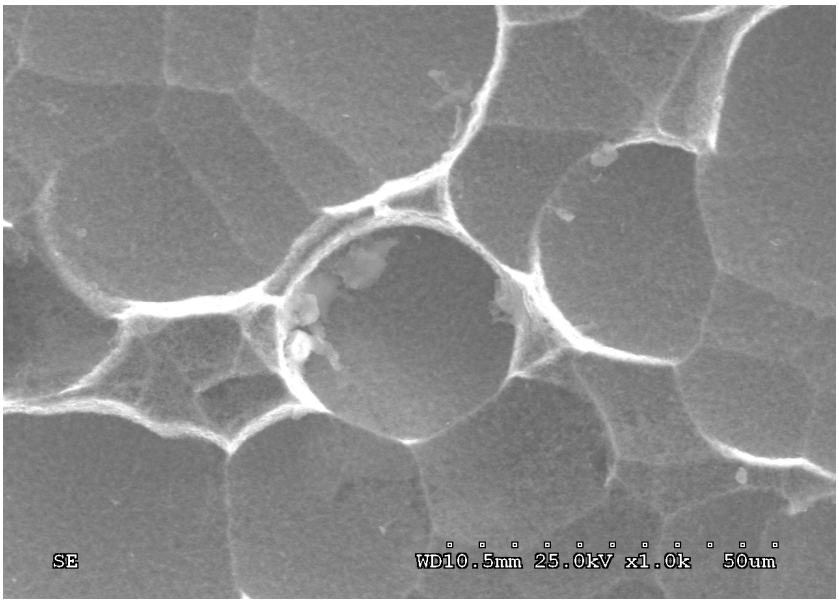

(a)

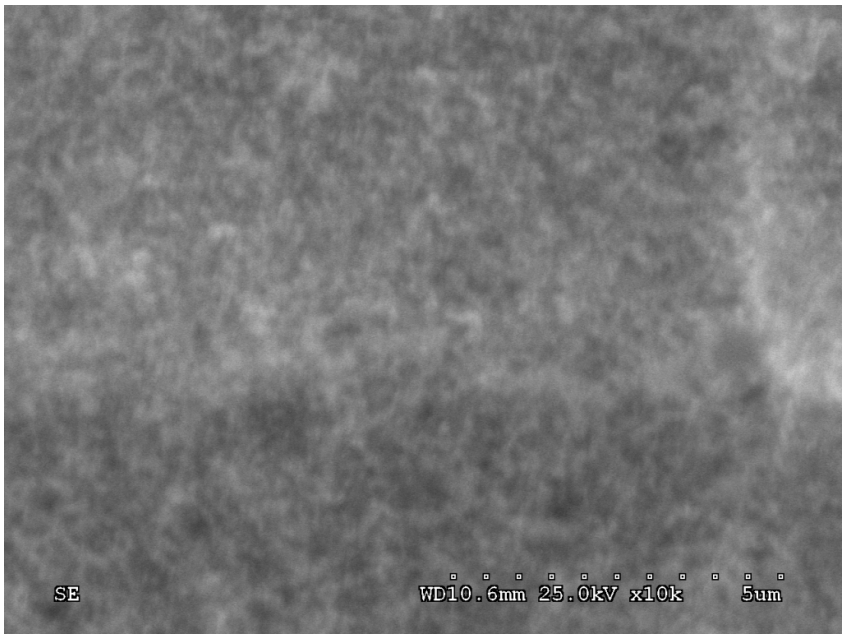

(b)

Figure 5.30 SEM micrographs showing the surface morphology of nano Ni after potentiodynamic polarization testing in 0.1N H_2SO_4 aerated solution showing formation of micro features (a) overview and (b) high magnification image of a micro feature.

5.3.5 Corrosion Potential in 0.1N H_2SO_4 Solution

Figure 5.31 presents the open circuit potential response of nano Ni in 0.1N H_2SO_4 aerated solution. The corrosion potential reaches a stable value around -250 mV in this environment. The value obtained from potentiodynamic polarization, Table 5.5, is in good agreement with the value observed in the OCP testing. Figure 5.32 shows the surface morphology of nano Ni. Very few, if any pits, can be observed in contrast to the bulk Ni where some small pits are clearly visible in Figure 5.17.

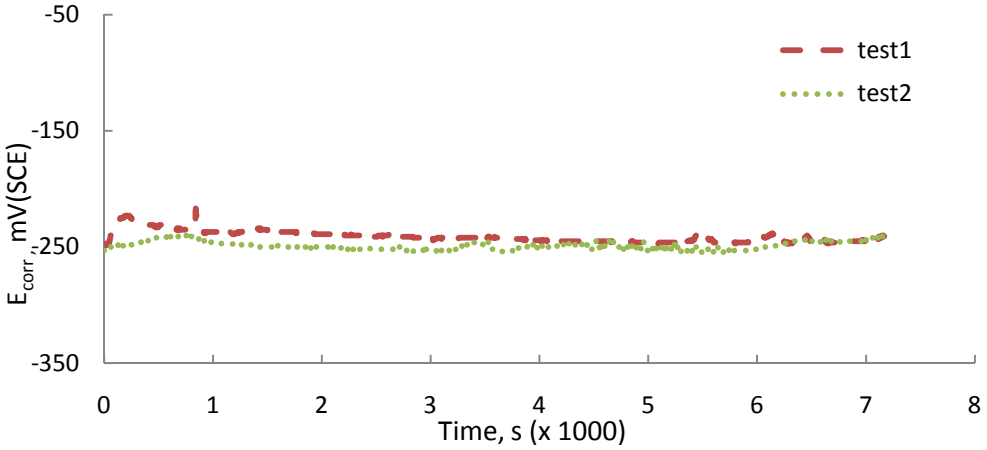

Figure 5.31 Open circuit potential response for nanocrystalline Ni in 0.1N H_2SO_4 aerated solution.

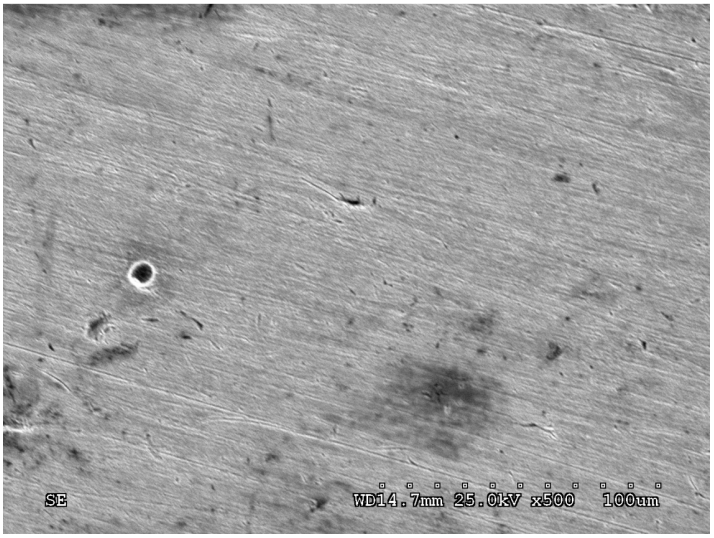

Figure 5.32 SEM micrograph showing surface morphology of nano Ni after open circuit potential vs. time testing in 0.1N H_2SO_4 aerated solution.

5.4 Comparison of Corrosion Behavior of Bulk and Nano Ni

5.4.1 Potentiodynamic Polarization Response of Bulk and Nano Ni in 3.5% NaCl Solution

Figure 5.33 presents the potentiodynamic response of bulk and nano Ni in aerated 3.5% NaCl solution. Both bulk and nano Ni display a similar activation polarization behavior but differ in their corrosion potential and corrosion current density values. There is a positive shift in the corrosion potential for the nano Ni and an increase in the corrosion rate. This is attributed to the catalytic reaction as nanocrystalline materials are known to have unique catalytic characteristics. These are the result of the high defect content in the form of interfaces and triple junctions [28]. The catalytic activation of the cathodic reaction will result in a higher exchange current density shifting the redox or corrosion potential and corrosion rate to higher values. As seen from Table 5.10, although the corrosion potential difference between the bulk and the nano Ni is only about 85 mV, the difference in current density value is significant. Nano Ni has an almost four fold higher corrosion current density when compared to its bulk counterpart. This is attributed to the higher concentration of grain boundaries and triple junctions in the nanocrystalline material which provide more preferential sites for electrochemical reaction resulting in a higher rate of the reduction reaction.

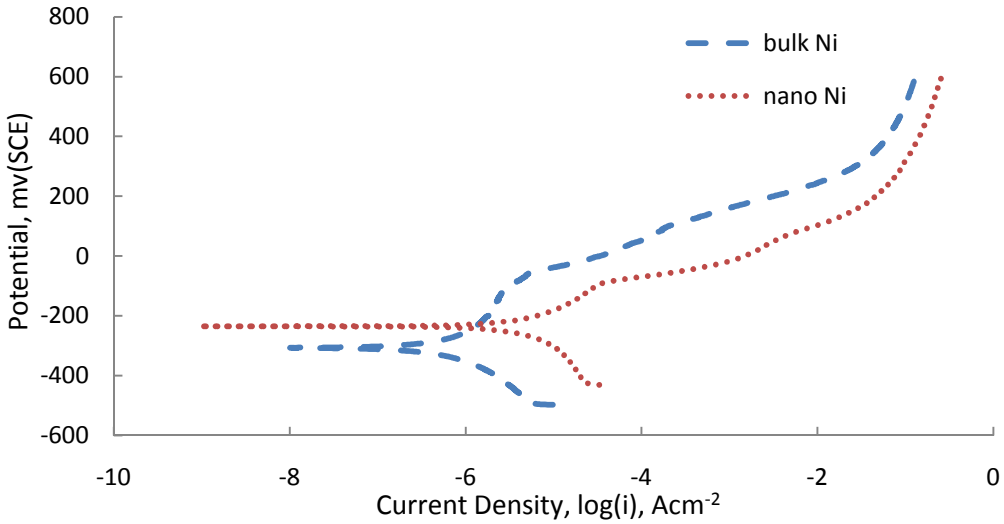

Figure 5.33 Comparison of potentiodynamic polarization behavior of bulk and nano Ni in 3.5% NaCl aerated solution.

It can be seen from Figure 5.34 and Table 5.11 that a similar response was obtained in the deaerated environment as that seen in the aerated environment for nano Ni in 3.5% NaCl solution. The corrosion potential for nano Ni is greater than that of the bulk as in the aerated solution. However, the corrosion current in nano Ni is smaller by almost one order of magnitude compared to that in bulk Ni unlike the response in aerated solution. In the absence of oxygen, catalytic reaction does not operate since cathodic reaction is different. This difference pronounces the role of grain boundaries in catalyzing the cathodic reaction.

Table 5.10 Comparison of Potentiodynamic Polarization Test Results for Bulk and Nano Ni in 3.5% NaCl Aerated Solution.

Parameter	Bulk	Nano
Corrosion Potential (mV)	-311.5	-227.4
Corrosion Rate ($\mu A.cm^{-2}$)	1.1	3.8

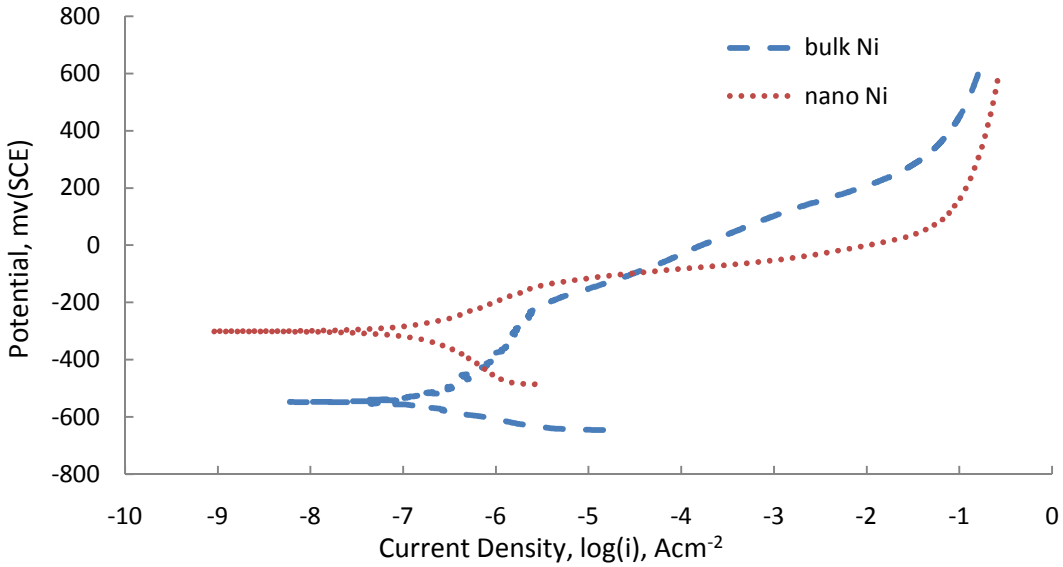

Figure 5.34 Comparison of the potentiodynamic polarization behavior of bulk and nano Ni in deaerated 3.5% NaCl solution.

Table 5.11 Comparison of Potentiodynamic Polarization Test Results for Bulk and Nano Ni in 3.5% NaCl Deaerated Solution.

Parameter	Bulk	Nano
Corrosion Potential (mV)	-553.13	-285.00
Corrosion Rate ($\mu A.cm^{-2}$)	0.27	0.03

5.4.2 Potentiodynamic Polarization Response of Bulk and Nano Ni in 0.1N H_2SO_4 Solution

Figure 5.35 shows the corrosion behavior of bulk and nano Ni in 0.1N H_2SO_4 aerated solution. Table 5.12 presents the corresponding values of corrosion potential and corrosion current. The bulk Ni is found to exhibit active-passive behavior, but the nano Ni under the same operating conditions exhibits activation polarization. From Table 5.12, the corrosion potential difference between the bulk and the nano Ni is around 60 mV, but there is almost five fold decrease in the current density. Due to higher number of grain boundaries and triple junctions formed on the highly disordered nanocrystalline Ni surfaces, a stable passive film is difficult to form [21, 26, 27].

The nanocrystalline Ni does not show passivation behavior in 0.1 N H_2SO_4 solution but shows passivation in 1N H_2SO_4 solution as observed for 2N H_2SO_4 solution in previous studies. The rate of passive film formation could be much lower than that observed in 2N H_2SO_4 due to slower cathodic reduction rate as the sites for electrochemical activity may require higher polarization potential to passivate. It was seen in previous studies in 2N H_2SO_4 [26] that the nanocrystalline Ni exhibited the same active-passive behavior typical of bulk Ni. It was also observed that nanocrystalline Ni shows higher current density in the passive region resulting in higher corrosion rate. Higher current density is attributed to higher grain boundary and tripe junction content in nanocrystalline Ni. The positive shift in the open circuit potential for nanocrystalline Ni is thought to be the result of catalysis of hydrogen evolution reaction. Such catalysis is expected to increase the exchange current density of the cathodic reaction. The highly defective film on the nanocrystalline material allows for a more uniform breakdown of the passive film which in turn leads to a more uniform corrosion. In coarse grained Ni, the breakdown of the passive film occurs first at grain boundaries and triple junctions rather than at crystal surface leading to preferential localized attack at these defects.

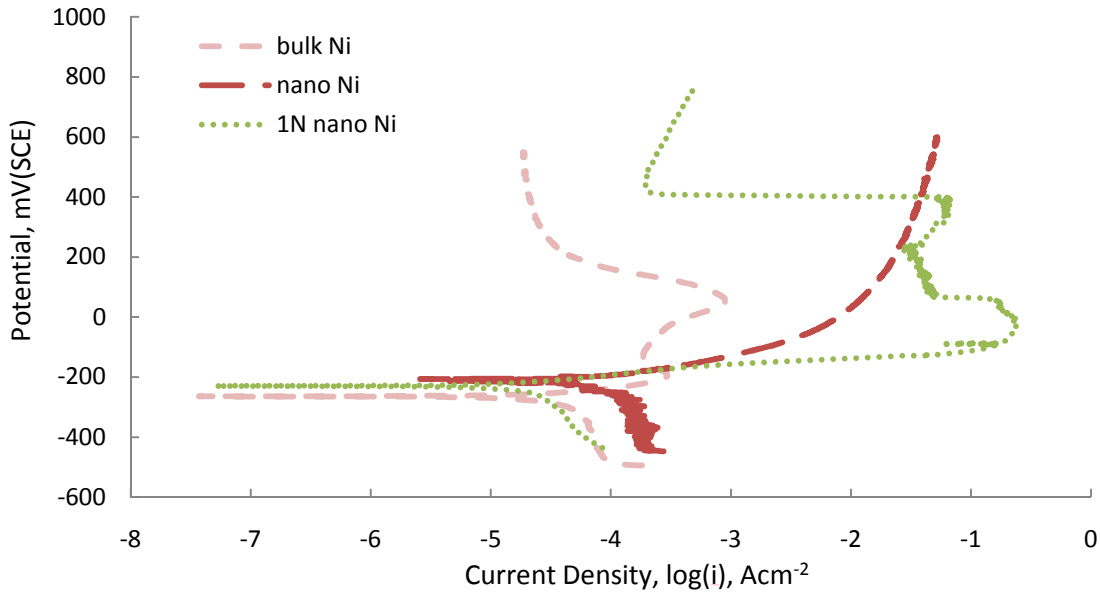

Figure 5.35 Comparison of potentiodynamic polarization behavior of bulk and nano Ni in 0.1N and 1N H_2SO_4 aerated solution.

Table 5.12 Comparison of Potentiodynamic Polarization Result of Bulk and Nano Ni in 0.1N H_2SO_4 Aerated Solution.

Parameter	Corrosion Potential (mV)	Corrosion Rate($\mu A.cm^{-2}$)
0.1N H_2SO_4 Bulk	-273.0	38
0.1N H_2SO_4 Nano	-211.6	211
1N H_2SO_4 Nano	-232.1	41.70

Figure 5.36 presents the potentiodynamic polarization behavior of bulk and nano Ni in 0.1N H_2SO_4 and 1N H_2SO_4 deaerated solution. Table 5.13 presents the corrosion potential and corrosion current density values for the bulk and nano Ni. Both exhibit similar corrosion potential and corrosion rate. They differ in the fact that passivation in nano Ni does not occur in 0.1N H_2SO_4 but passivation is observed in 1N H_2SO_4 solution. The passive film formation rate in a diluted H_2SO_4 is not sufficient to cause passivation in nano Ni in the presence of the large density of surface defects.

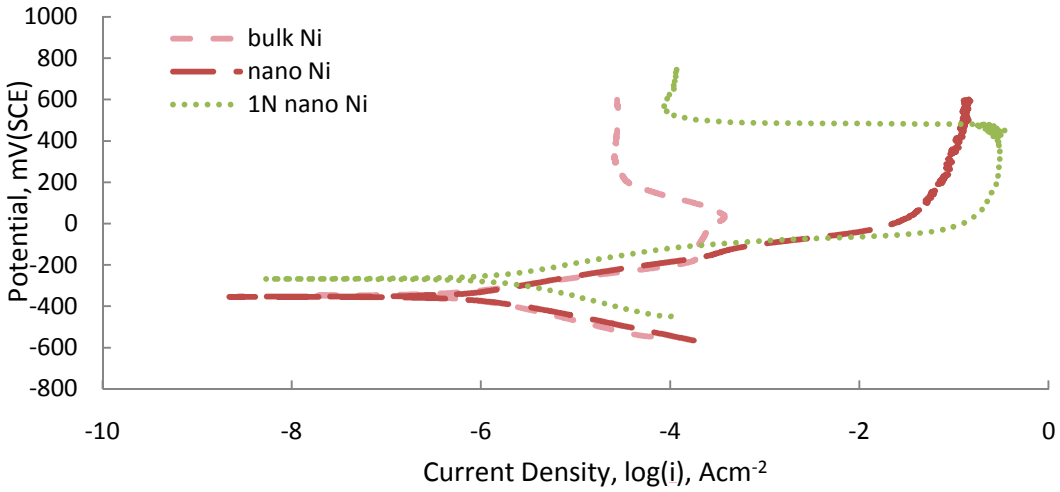

Figure 5.36 Comparison potentiodynamic polarization behavior of bulk and nano Ni in 0.1N H_2SO_4 deaerated solution.

Table 5.13 Comparison of Potentiodynamic Polarization Test Result of Bulk and Nano Ni in 0.1N H_2SO_4 Deaerated Solution.

Parameter	Corrosion Potential (mV)	Corrosion Rate($\mu A.cm^{-2}$)
0.1N H_2SO_4 Bulk	-355.0	1.1
0.1N H_2SO_4 Nano	-353	2.1
1N H_2SO_4 Nano	-266.1	1.4

5.4.3 Open Circuit Response of Bulk and Nano Ni

Figures 5.37 and 5.38 present the open circuit potential response of bulk and nano Ni in 3.5% NaCl and 0.1 N H_2SO_4 aerated solutions, respectively. It can be observed that both bulk and nano Ni attain equilibrium at similar corrosion potentials, but the nano Ni, exhibits a somewhat more noble corrosion potential in agreement with the anodic polarization findings.

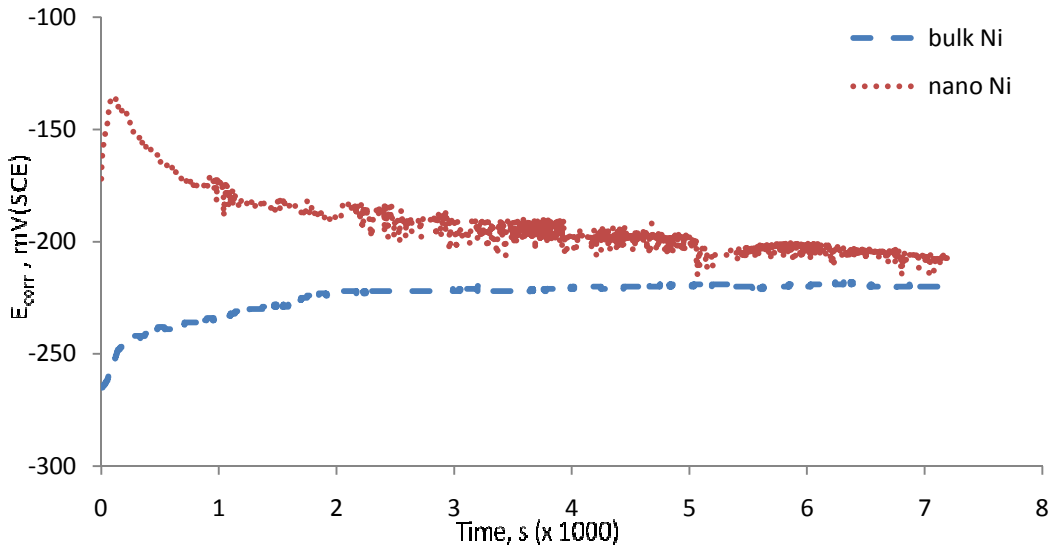

Figure 5.37 Comparison of open circuit potential as a function of time for bulk and nano Ni in 3.5% NaCl aerated solution.

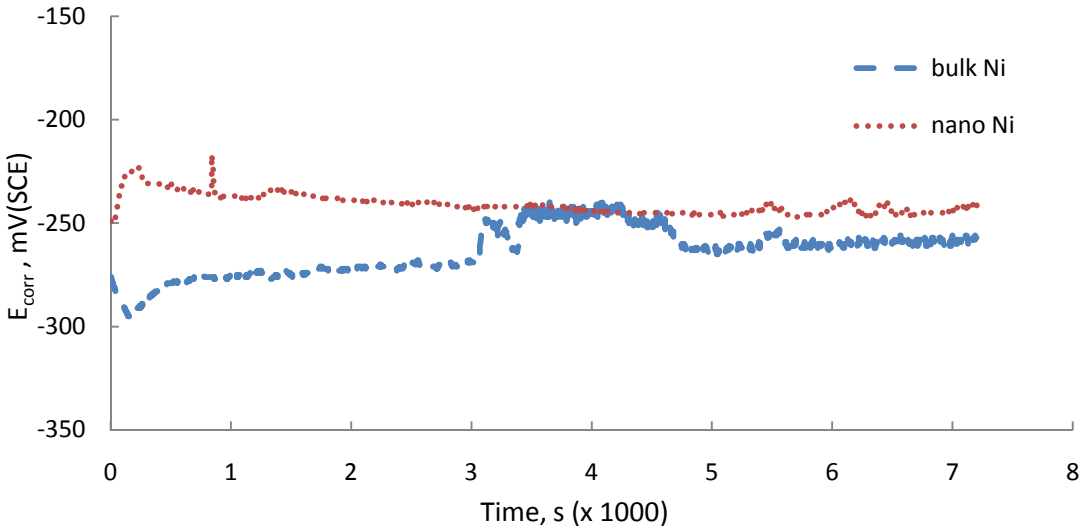

Figure 5.38 Comparison of open circuit potential as a function of time for bulk and nano Ni in 0.1N H_2SO_4 aerated solution.

In summary, nano Ni was found to exhibit a more noble potential in both NaCl and H_2SO_4 solutions. In aerated environments, the corrosion rate of nano Ni is higher than that of bulk Ni. This is attributed to the catalytic properties for oxygen reduction by the large volume fraction of grain boundaries present in nano Ni. In deaerated solutions, nano Ni exhibits either a significantly lower (i.e., NaCl solution) or comparable (i.e., 0.1N H_2SO_4 solution) corrosion rate to that of its microcrystalline counterpart.

It should be noted that in the latter case, the corrosion rate for bulk and nano Ni is comparable. Furthermore, the present results show that in the presence of dilute H_2SO_4 solution, nano Ni does not passivate more than likely due to a lower cathodic reaction rate that is not sufficient to drive up the oxidation potential and build a stable oxide. A higher cathodic reduction reaction rate available in concentrated H_2SO_4 is required to passivate nano Ni as seen in 1N H_2SO_4 solution.

In terms of surface morphology in NaCl solution, pits in nano Ni were found to be uniform in depth (40 to 45 μm), whereas in microcrystalline Ni showed a large variation extending to a depth of 59 μm). In the diluted H_2SO_4 solution, corrosion for nano Ni was found to be rather uniform since a passive film was not present. This new evidence suggests that the catalytic effect

by the nano Ni structure is pronounced only for the reduction of O_2. In the absence of oxygen, both corrosion rates are similar. As far as the reduction of H^+ is concerned, the present results do not indicate any particular catalytic effect by the nano Ni. It is noted that in the absence of oxygen, the corrosion rate of bulk and nano Ni in H_2SO_4 was similar. The reasons for the enhanced reduction reaction observed by nano Ni in aerated electrolytes are not known. Such an enhancement can be attributed to better adsorption of oxygen molecules at the nanostructured Ni surface in view of the higher density of grain boundaries. Such sites can serve as anchor locations for O_2 adsorption and facilitate electron transfer resulting in significant enhancement of cathodic reaction rate.

CHAPTER 6

CONCLUSIONS

The conclusions of the present study were:

I. Nanocrystalline Ni exhibited more noble potential than its bulk counterpart in both 3.5% NaCl and 0.1N H_2SO_4 electrolytes tested.

II. In aerated solutions, nano Ni exhibited significantly higher corrosion rate than bulk Ni. This behavior was attributed to the catalysis of the oxygen reduction reaction by the high density of grain boundaries present on the nano Ni.

III. In deaerated solutions, nano Ni exhibited either a significantly lower (i.e., in 3.5% NaCl solution) or comparable (i.e., in 0.1N H_2SO_4 solution) corrosion rate to that of its microcrystalline counterpart. This behavior clearly suggests that the catalytic activity by the nano Ni surface is present only for oxygen and not for hydrogen reduction reactions.

IV. In diluted H_2SO_4 solution, bulk Ni passivated whereas nano Ni was not able to develop a stable passive film in view of the high density of surface defects arising from the large fraction of grain boundaries.

V. Surface morphology analysis revealed pitting corrosion of microcrystalline Ni in NaCl and H_2SO_4 solutions. Since microcrystalline Ni passivates in 0.1N H_2SO_4 solution, the attack in 0.1N H_2SO_4 solution was less intense in comparison to the corrosion in 3.5% NaCl solution.

VI. Pits in nano Ni when tested in 3.5% NaCl solution were found to be uniform in depth ~ 42 μm, whereas the microcrystalline Ni showed a larger variation extending to a depth of 59μm. A bimodal pit distribution was observed with a larger number of submicron pits nucleating at grain boundaries but with only a small fraction growing to form larger pits. An interesting observation was made for the first time with pits exhibiting vertical but also

lateral growth producing a characteristic pit appearance. In the dilute H_2SO_4 solution, corrosion for nano Ni was found to be rather uniform since a passive film was not present.

REFERENCES

[1] H. Gleiter, Acta Materialia 48, 2000 (1991).

[2] S.C. Tjong, H. Chen, Material Science and Engineering R 45, 1-88 (2004).

[3] S.H. Kim, Corrosion Properties of Nanocrystalline Nickel and Cobalt Electrodeposits, Ph.D. Thesis, University of Toronto, Canada (2004).

[4] G. Palumbo, S.J. Thorpe, K.T. Aust, Scripta Metallurgica 24, 1247 (1990).

[5] Jones D.A, (1996). Principles and Prevention of Corrosion. Upper Saddle River, New Jersey. Prentice Hall. ISBN-13:3599930.

[6] U. Erb, G. Palumbo, D. Jeong, S. Kim, K.T. Aust, Processing and Properties of Structural Nanomaterials, Eds. by L. Shaw et al., The Minerals, Metals and Materials Society, (2003).

[7] Banks D. (2006). Micorengineering, MEMS and Interfacing. 6000 Broken Sound Parkway NW, Suite 300 Boca Raton, FL 334872742. ISBN-13: 9780824723057.

[8] Nickel Institute, reprint series number 14084.

[9] D.J. Guidry, K. Lian, J.C. Jiang and E.I. Meletis, Journal of Nanoscience and Nanotechnology 9(7), 4156-4163 (2009).

[10] S.C. Mehta, D.A. Smith and U. Erb, Material Science and Engineering A 204, 227 (1995).

[11] K.S. Kumar, S. Suresh, M.F. Chisholm, J.A. Horton, P. Wang, Acta Materialia 51, 287 (2003).

[12] B.D. Cullity, (1956). Elements of X-ray Diffraction. Wesley Publishing Company, Addision NJ. ISBN-13: 9780201610918.

[13] H. Gleiter, Progress in Material Science 33, 223 (1989).

[14] U. Erb, G. Palumbo, R. Zugic, K.T. Aust, Processing and Properties of Nanocrystalline Materials, Eds. by J. Singh and F.H. Froes, The Minerals, Metals and Materials Society, (1996).

[15] U.Erb, K.T. Aust and G. Palumbo, Nanostructured Materials – Processing, Properties and Potential Applications, Eds. by C.C. Koch, Noyes Publications, William Andrew Publishing, Norwich, New York, 179 (2002).

[16] U. Erb, K.T. Aust, G. Palumbo, J. Mc Crea and F. Gonzalesz, Processing and Fabrication of Advanced Materials IX, Eds. by T.S. Srinivasan et al., ASM International, Materials Park, OH, 253 (2001).

[17] A.M. El-Sherik and U. Erb, Applications and Materials Performance, Eds. By F.N. Smith et al., The Metallurgical Society of CIM, Montreal, PQ (1997).

[18] D.H. Jeong, F. Gonzalez, G. Palumbo, K.T. Aust and U. Erb, Scripta Materialia 44, 493 (2001).

[19] Y. Zhou, U. Erb, G. Palumbo and K.T. Aust, Zeitschrift Fur Metallkunde 94, 1157 (2003).

[20] G.A. Cragnolinio, (2008). Corrosion Fundamentals and Characterization Technique, Woodhead Publishing Limited, 80 High Street Sawston CB22 3HJ UK. ISBN-13:9781845691875.

[21] S. Wang, Electrochemical Properties of Nanocrystalline Ni and Ni-Mo Alloys, Ph.D. Thesis, Queen's University, Kingston, Ontario, Canada (1997).

[22] R. Rofagha, S.J. Splinter, U. Erb and N. S. Mc Intyre, Nanostructured Materials 6, 1013 (1995).

[23] W. Zeigher, M. Schneider, D. Schenweber and H. Worch, Nanostructured Materials 6, 1013 (1995).

[24] M.D. Merz, Metallurgical and Materials Transactions 10A, 71 (1979).

[25] D.R. Baer and M.D. Merz, Metallurgical and Materials Transactions 11A, 1973 (1980).

[26] Z. Szklarska-Smialowska, S. Shademan and R. Inturi, Materials Science Forum 185-188, 1011 (1995).

[27] R. Rofagha, R. Langer, A.M. El-Sherik, U. Erb, G. Palumbo and K.T. Aust, Scripta Metallurgica et Materialia 25, 2867 (1991).

[28] R. Rofgha, R. Langer, A.M. El-Sherik, U. Erb, G. Palumbo and K.T. Aust, Materials Research Society Symposium Proceeding 238, 751 (1992).

[29] A.M. El-Sherik and U. Erb, Plating and Surface Finishing 82, 85 (1995).

[30] P.T. Tang, T. Watanabe, J.E.T. Andersen and G. Bech-Nieslen, Journal of Applied Electrochemistry 25, 347 (1995).

[31] S. Wang, R. Rofagha, P.R. Robergue and U. Erb, Electrochemical Society Proceedings 95-8, 244 (1995).

[32] R.A. Mirshams, P. Parkala, Materials Science and Engineering A372, 252-260 (2004).

BIOGRAPHICAL INFORMATION

Anjana Shyamsundar was born in Bangalore, India. She received a Bachelor of Engineering in Chemical Engineering degree in 2007, from MSRIT, Bangalore- India. To explore and understand the theory behind the unique structure and property of materials, she decided to pursue a Master of Science degree in materials science and engineering, at the University of Texas, Arlington in 2008. She also started her research work under the able guidance of Dr. Efstathios I. Meletis.

While attending school, apart from working on her research, Anjana also worked part time on campus, as a Community Service Officer for the University of Texas Arlington, Police Department. Anjana's research interests include electrochemistry, surface analysis, solid state device theory and applications.